

Modeling ice-shelf cavities using Lagrangian elements

A.A. Stern,¹, A. Adcroft¹ and O. Sergienko¹, G. Marques¹, R. Hallberg¹

Key Points:

3

- 4 • A novel modeling framework is developed to model breakable ice shelves and ice-shelf cavities
- 5 using Lagrangian elements, held together by numerical bonds.
- 6 • The ocean circulation beneath a (static) Lagrangian ice shelf is almost indistinguishable
- 7 from the circulation beneath an Eulerian ice-shelf model run in an identical configuration, which
- 8 provides a proof of concept for the Lagrangian model.
- 9 • After an iceberg calves away from an ice shelf, a complex interaction is observed between
- 10 the iceberg motion and ocean hydrography. This interaction leads to the formation of a Taylor
- 11 column beneath the iceberg, a subsurface cooling at the ice front, and reduced melt rates within
- 12 the ice shelf cavity.

A. A. Stern, Geophysical Fluid Dynamics Laboratory, Princeton University

A. Adcroft, Geophysical Fluid Dynamics Laboratory, Princeton University

O. Sergienko, Geophysical Fluid Dynamics Laboratory, Princeton University

G. Marques, Geophysical Fluid Dynamics Laboratory, Princeton University

R. Hallberg, Geophysical Fluid Dynamics Laboratory, Princeton University

13 Abstract. The current generation of ice-ocean models is unable to rep-
14 resent ice-shelf calving in a physically realistic way, despite the controlling
15 role that calving plays in the setting mass balance and extent of Antarctic
16 ice shelves. The infrequency of large calving events together with the diffi-
17 culty of placing observational instruments around tabular icebergs means that
18 little is known about how calving icebergs affect the ocean. In this study we
19 present a novel model of an ice-shelf cavity below a breakable ice shelf con-
20 structed of Lagrangian elements. We validate the Lagrangian ice shelf model
21 by simulating the flow beneath a (static) idealized ice shelf, and comparing
22 the results to an Eulerian model simulations with identical configuration. The
23 Lagrangian model is then used to simulate the ocean's response to a tabu-
24 lar iceberg calving away from the ice shelf. The results show a calving ice-
25 berg can lead to large changes in the surrounding ocean. Changes in circu-
26 lation patterns and enhanced vertical mixing are observed at the ice front
27 and around the iceberg following the calving event. The vertical mixing at
28 the ice front warms the ocean surface and cools the water column at depth,
29 allowing cooler waters to enter the ice shelf cavity, which in turn leads to re-
30 duced melt rates within the cavity. A Taylor column is observed below the
31 iceberg, which moves with the iceberg as it drifts into the open ocean. As
32 the tabular iceberg drifts further from the ice shelf, the circulation within
33 the ice shelf cavity tends towards a new steady state, consistent with the new
34 ice shelf geometry.

1. Introduction

Satellite observations show that ice-shelf decay occurs via two main processes: melting and breaking [Depoorter et al , 2013; Rignot et al , 2013]. Each of these is responsible for approximately half of the ice-shelf decay, and each influences the surrounding ocean (and ice-shelf geometry) in a distinct way. Melting at the base of ice shelves causes fluxes of freshwater into the ice-shelf cavity. The input of buoyant meltwater creates rising density plumes, which are guided along the ice-shelf base, and help drive ocean circulation beneath the ice shelves [MacAyeal , 1984; Holland and Feltham , 2006]. Over time, melting at the ice-shelf base can erode the ice shelf, gradually altering the ice-shelf geometry. In contrast, iceberg calving causes sudden changes to the ice-shelf geometry, and releases giant icebergs into the ocean. After calving, these tabular icebergs can travel large distances and impact ocean hydrography [Martin and Adcroft , 2010; Stern et al , 2015], sea-ice formation [Robinson and Williams , 2012; Stern et al , 2016] and ocean biology [Smith et al , 2007; Vernet et al , 2012; Biddle et al , 2015] many miles away.

Modeling the ocean beneath the ice shelves presents a unique set of challenges, since (i) the presence of ice shelves provides a quasi-rigid upper boundary for the ocean model which is not encountered elsewhere in the ocean, and (ii) melting and breaking ice shelves imply changing ocean boundary conditions which present numerous numerical difficulties.

The earliest models of ocean ice-shelf cavities were developed using static ice shelves with a fixed shape [Hellmer and Olbers , 1989; Determan and Gerdes , 1994; Grosfeld et al , 1997; Holland and Jenkins , 2001; Losch , 2008]. In these models, ice-shelf melting was represented through salinity and temperature fluxes, while the ice-shelf geometry

56 remained unchanged. Later models of ice-shelf cavities allowed the ice-shelf geometry
57 to evolve as the ice shelf melted, permitting the study of coupled ocean-ice phenomena
58 [Gladish et al , 2012; Sergienko , 2013]. More recently, dynamic ice-shelf models have
59 been coupled to the ocean cavity, allowing the study of grounding line migration which is
60 of key importance for sea level rise projections [Grosfeld and Sandhger , 2004; Goldberg
61 et al , 2012; De Rydt and Gudmundsson , 2016; Seroussi et al , 2017].

62 All models of ice-shelf cavities to date have omitted ice-shelf breaking and iceberg
63 detachment. This is because (i) there is much uncertainty about the physics that govern
64 ice-shelf breaking [Benn et all , 2007; Alley et al , 2008; Levermann et al , 2012; Bassis
65 and Jacobs , 2013], and (ii) current models of ice-shelf cavities represent the ice shelves on
66 static Eulerian grids, which do not lend themselves to modeling iceberg detachment and
67 drift. In contrast, existing *iceberg* models represent icebergs as Lagrangian particles, since
68 this is a convenient way to model discrete objects traveling over large distances [Bigg et
69 al , 1997; Gladstone et al , 2001; Martin and Adcroft , 2010; Marsh et al , 2015]. To date
70 there has been no real effort to synthesize these two approaches (i.e.: to combine ice shelf
71 and iceberg models).

72 In this study we develop a new ice-shelf cavity model where the ice shelf is simulated
73 with Lagrangian elements [Stern et al , 2017]. In this model, the ice shelf is constructed
74 out of Lagrangian elements which are bonded together by numerical bonds (see schematic
75 Figures 1). This Lagrangian framework allows for large pieces of the ice shelf to break away
76 and become tabular icebergs. An example of this enhanced capability of the Lagrangian
77 model is demonstrated in Figures 2, which shows a tabular iceberg drifting away from an
78 idealized ice shelf.

79 The goals of this study are (i) to introduce and describe the Lagrangian ice-shelf model,
80 (ii) to validate the Lagrangian model by simulating the flow beneath a static idealized
81 ice shelf cavity, and comparing it to an Eulerian ice-shelf model run in an identical con-
82 figuration, and (iii) to demonstrate the enhanced capabilities of the Lagrangian ice-shelf
83 model by simulating a large iceberg calving away from the idealized ice shelf. Modeling
84 the ocean during and after a calving event, allows us to observe how the calving event
85 affects the ocean near and beneath the ice shelf, and how changes in the ocean feedback
86 onto the ice shelf.

2. Lagrangian model description

87 The Kinematic Iceberg Dynamics (KID) model is a Lagrangian model that has been
88 developed in order to simulate ice-shelf cavities with breakable ice shelves. The model
89 represents ice shelves using Lagrangian elements joined together by numerical bonds. By
90 breaking these bonds, the model is able to simulate ice-shelf calving and iceberg breakup.

91 In this section we describe the Lagrangian ice-shelf model. A more complete description
92 of the model including numerical methods and algorithms used to track the numerical
93 bonds can be found in Stern et al [2017].

2.1. Kinematic Iceberg Dynamics model

94 The KID model is a Lagrangian particle-based model, in that the objects of the model
95 are Lagrangian elements. Each Lagrangian element represents a column of ice that is
96 floating in the ocean. The elements have their own position, velocity, mass, and a set
97 of dimensions, which can evolve in time. Each element moves according to its own mo-
98 mentum balance which is computed in the (Lagrangian) reference frame of the element.

99 The elements experience oceanic, sea ice and atmospheric drag forces, as well as a forces
 100 due to sea surface height gradients, and the Coriolis force [Bigg et al , 1997; Gladstone
 101 et al , 2001; Martin and Adcroft , 2010; Stern et al , 2017]. The elements also interact
 102 with other elements and can be ‘bonded’ together by numerical bonds, which allow many
 103 elements to move together as a unit. By bonding many ice elements together, the model
 104 is able to form larger structures, such as tabular icebergs or ice shelves (Figure 1).

2.2. Equations of motion

The momentum equation for each element is given by

$$M \frac{D\vec{u}}{Dt} = \vec{F}_A + \vec{F}_W + \vec{F}_R + \vec{F}_C + \vec{F}_{SS} + \vec{F}_{SI} + \vec{F}_{IA}, \quad (1)$$

105 where $\frac{D}{Dt}$ is the total (Lagrangian) derivative, M is the mass of the element, \vec{u} is the
 106 velocity of the element, and the terms on the right hand side give the forces on the
 107 element due to air drag (\vec{F}_A), water drag (\vec{F}_W), sea-ice drag (\vec{F}_{SI}), Coriolis force (\vec{F}_C),
 108 wave radiation force (\vec{F}_R), sea surface slope (\vec{F}_{SS}), and interactions with other elements
 109 (\vec{F}_{IA}).

110 The forces on each element are set up such that in the absence of interactive forces,
 111 the ice elements follow the same equations used in iceberg drift models [Bigg et al , 1997;
 112 Gladstone et al , 2001; Martin and Adcroft , 2010]). This ensures that when an element
 113 breaks away from an ice shelf and drifts in the open ocean, it is modeled as a freely drifting
 114 iceberg. When an element is connected to the ice shelf (or larger ice structure), it also
 115 experiences forces due to interactions with the elements around it. The details of these
 116 interactive forces between elements are described below. A complete description of the
 117 other forces acting on the iceberg is provided in Stern et al [2017].

2.3. Interactive Forces

Interactive forces are applied between elements to prevent elements overlapping with neighboring elements, and prevent ‘bonded’ elements from moving apart from one another (see Figures 1a). The interactive forces are modeled as damped elastic forces: For two elements i and j at positions \vec{x}_i and \vec{x}_j , the elastic and damped components of the interactive force are given by

$$(\vec{F}_e)_{ij} = -\kappa_e \left(d_{ij} - L_{ij} \right) M_{ij} \vec{r}_{ij}, \quad (2)$$

and

$$(\vec{F}_d)_{ij} = -M_{ij} c_{r_{||}} P_{\vec{r}_{ij}} \cdot (\vec{u}_i - \vec{u}_j), \quad (3)$$

₁₁₈ respectively. Here $d_{ij} = |\vec{x}_i - \vec{x}_j|$ is the distance between the elements, $\vec{r}_{ij} = \frac{(\vec{x}_i - \vec{x}_j)}{|\vec{x}_i - \vec{x}_j|}$ is the
₁₁₉ directional unit vector between element. L_{ij} is the average diameter of the two elements
₁₂₀ (assuming a circular shape for the elements), κ_e is the spring constant, and M_{ij} is the
₁₂₁ minimum of the masses of elements i and j . $P_{\vec{r}_{ij}}$ is the projection matrix that projects
₁₂₂ onto \vec{r}_{ij} , and $c_{r_{||}}$ is the drag coefficient. We set $c_{r_{||}} = 2\sqrt{\kappa_e}$, so that the elastic force is
₁₂₃ critically damped. The total interactive \vec{F}_{IA} on an element is found by summing up the
₁₂₄ all the interactive forces with other elements.

2.4. Melt rates

₁₂₅ The thickness and extent of the Lagrangian elements change due to melting when they
₁₂₆ are exposed to above-freezing ocean mixed-layer temperatures. The melt rates of the
₁₂₇ elements in the interior of a large structure (such as an ice shelf or large icebergs) are
₁₂₈ parametrized using the three-equation model, which is a typically melt rate parametriza-
₁₂₉ tion used to model basal melt beneath ice shelves [Holland and Jenkins, 1999]. The melt

130 rates of freely floating ice elements (not bonded to other elements) are parametrized using
131 standard parametrizations for iceberg [Bigg et al , 1997; Gladstone et al , 2001; Martin
132 and Adcroft , 2010]. For elements at the edge of large structures (with edges partly ex-
133 poses to the open ocean) the melt rates are computed using a weighted sum of the ice
134 shelf and and iceberg melt rate parametrization, with the weights being proportional to
135 the fraction of the element's perimeter which exposed to the open ocean [Stern et al ,
136 2017].

2.5. Initializing element geometry and packing

137 The elements in the Lagrangian model are shaped as equally-sized regular hexagons (al-
138 though they are treated as circular for the purpose of element interactions). We initialize
139 the Lagrangian model by positioning the elements in a staggered lattice of equally-size
140 hexagons, so that the elements fit together and perfectly tile the ice-shelf surface (Figures
141 1). Hexagonal elements are used so that when adjacent pairs of elements are bonded to-
142 gether, the network of bonds form equilateral triangles, which gives rigidity to the larger
143 structure [Stern et al , 2017]. By using hexagonal elements, which can be packed to-
144 gether without any gaps, the element initialization is perfectly space filling. This allows
145 the model to simulate continuous ice shelves (without gaps or crevasses), and allows the
146 results to be more easily comparable with Eulerian ice shelf models. In this study, we
147 only use hexagonal elements, however, other element geometries, can be used when less
148 precision is needed.

2.6. Interpolation and aggregation onto the Lagrangian grid

At every time step, ice-shelf fields are passed from the ice-shelf model to the ocean model and from the ocean model to the ice-shelf model. Fields which are passed from the ocean model to the Lagrangian ice shelf model have to be interpolated from the Eulerian grid onto the Lagrangian grid (i.e.: onto the elements). This is done using a bilinear interpolation scheme. Four ocean fields are passed from the ocean model to the ice-shelf model: temperature, salinity and zonal and meridional velocities.

At the end of an ice-shelf model time step, ice-shelf fields are aggregated from the elements back onto the Eulerian ocean grid, and are then passed from the ice-shelf model to the ocean model. The aggregation from the Lagrangian elements onto the Eulerian grid is done by calculating the fraction of each element's volume that lies in each ocean grid cell, and dividing the fields in proportion to this fraction. For example, the amount of ice mass aggregated onto a given ocean grid cell is found by summing up the masses of all elements which intersect that grid cell, only counting the part of an element's mass that actually intersects the ocean grid cell. When calculating the intersection between an element and a grid cell, we assume that the elements have surface areas that are shaped as regular hexagons. Seven fields are passed from the ice-shelf models to ocean model: iceberg mass and surface area (used to calculate the upper-ocean pressure field), temperature flux, salinity flux and mass flux, and meridian and zonal velocity (used to calculate the momentum flux).

3. Experiment setup

3.1. Domain configuration

In order for our simulations to be easily comparable to previous models of ice-shelf cavities, we use an experimental setup based on the configuration created for the Marine Ice Ocean Modeling Inter-comparison Project (MISOMIP) [Asay-Davis et al , 2016]. The configuration consists of an idealized ice shelf in a rectangular domain $L_x = 80\text{km}$ long and $L_y = 480\text{km}$ wide. The ice shelf is grounded on the southern side of the domain with the ice-shelf front at $y=650\text{km}$. The ice thickness and bottom topography of this setup are shown in Figure 3. The configuration is the same as that of the Ocean0 setup in the MISOMIP, with three changes made:

1. The ‘calving criteria’ used in the MISOMIP study (which states that all points in the ice shelf with thickness less than 100m are set to zero thickness) has not been used.
2. The ice shelf has been thickened on the flanks of the domain, so that the latitude of the grounding line increases away from the center of the ice shelf.
3. The ice shelf is configured to be symmetric about its meridional center line ($x = \frac{L_x}{2}$). This was achieved by using the average of the left and right flanks of the ice-shelf thickness. These three changes were made in order to make the circulation beneath the ice shelf easier to interpret.

3.2. Ocean model

The Lagrangian and Eulerian ice shelves are coupled to the MOM6 ocean model [Hallberg et al , 2013]. The ocean model is run using a hybrid vertical coordinate system which blends a sigma-level and a z-level coordinate [Stern et al , 2017], implemented using the ALE method [White et al , 2009]. In this vertical coordinate, model layers bend

underneath surface topography (i.e.: the ice shelf), as they would in a sigma coordinate model, and intersect the bottom topography, as they would in a z-coordinate model. The model has 72 vertical layers and has a horizontal resolution of $\Delta x = 2$ km. The numerical simulations were all repeated using an isopycnal coordinate (without ALE regridding-remapping). The results were qualitatively similar to the hybrid-coordinate results, and are therefore not presented here.

The ocean parameters used in the simulations are as specified in the MISOMIP configuration [Asay-Davis et al , 2016], and are shown in Table 1. The simulation is initialized from rest, with horizontally uniform initial ocean temperature and salinity profiles which vary linearly between specified open-ocean surface and bottom values: $T_{top} = -1.9^{\circ}\text{C}$, $T_{bottom} = 1.0^{\circ}\text{C}$, $S_{top} = 33.8$ psu, $S_{bottom} = 34.7$. The maximum ocean depth is $H_{ocean} = 720$ m. A sponge layer is used on the northern boundary, which relaxes back to the initial temperature and salinity with a relaxation time scale of $T_{sponge} = 0.1$ days over a distance of 10 km. Melting is set to zero for ocean cells where the ocean column thickness is less than 10m.

3.3. Lagrangian ice-shelf model:

The Lagrangian ice-shelf simulations are performed using the Kinematic Iceberg Dynamics (KID) model described in Section 2. The Lagrangian ice shelf is created using 10882 Lagrangian hexagonal elements with sides of length $S = 0.98$ km . The positions of the hexagonal elements are initialized by packing them together in a space-filling staggered lattice. Gaps along the boundaries are filled in using smaller elements so that the total ice-shelf area is preserved. The initial mass of the ice elements is determined using bilinear interpolation from a prescribed gridded ice mass field.

3.4. Eulerian ice-shelf model:

210 The Eulerian ice-shelf simulation is performed using an existing Eulerian ice-shelf cavity
 211 model [Goldberg et al , 2012], which is an optional module of the the MOM6 ocean model.
 212 The ice shelf is initialized on the same grid as the ocean model with a horizontal resolution
 213 of $\Delta x = 2$ km. The ice-shelf thickness field is initialized using the same ice-shelf draft used
 214 for the Lagrangian model (Figure 3). The melt rates in the Eulerian ice-shelf simulation
 215 are calculated using the 3 equation model for ice-shelf decay [Holland and Jenkins, 1999],
 216 with the same parameters used to calculate the ice shelf melt rates in the Lagrangian
 217 model.

4. Model validation

218 The Lagrangian ice shelf model is validated by comparing it to an existing Eularian ice
 219 shelf model in an identical static configuration.

4.1. Setup of static validation experiment:

220 The experimental setup for the model validation experiment is based on the Ocean0
 221 MISOMIP experiment [Asay-Davis et al , 2016]. In this experiment the ice shelves are
 222 thermodynamically active but have a time-invariant thickness. Temperature and salinity
 223 fluxes from ice shelf melt drive the circulation within the cavity.

224 A constant wind stress $\vec{\tau} = \langle \tau_x, \tau_y \rangle = \langle 0.05, 0.05 \rangle \frac{N}{m^2}$ is applied to the ocean surface.

225 Note that this wind stress is was not applied in the original MISOMIP experiments [Asay-
 226 Davis et al , 2016].

227 The elements in the Lagrangian ice shelf simulation are held stationary so that the ice
228 shelf is static and comparable to the Eulerian simulation. The models are spun up for 5
229 years. The analysis is performed on year 6 to 10 of the simulations.

4.2. Results of validation experiment

230 The results of the static ice shelf simulations in both simulations are qualitatively similar
231 to results presented in [Asay-Davis et al , 2016]. Melting at the base of the ice shelf drives
232 a circulation within the cavity and strong jets are observed at the ice front and along the
233 sides of the domain (Figure 4). A more complete description of the circulation is provided
234 in the supplementary material.

235 Since the Lagrangian and Eulerian ice shelf models are coupled to the same ocean model
236 and the ice shelf models use the same parametrization for ice shelf melt, we expect the
237 results of the two models to be the almost the same, with the only differences arising from
238 the interpolation and aggregation schemes (see Section 2.6). The results show that two
239 simulations are almost indistinguishable. This is demonstrated, for example, in Figure
240 4, which shows the time-averaged barotropic stream function of the Lagrangian (Figures
241 4a) and Eulerian (Figures 4b) simulations, and the difference between the two (Figures
242 4c). The difference between the Lagrangian and Eulerian barotropic stream functions are
243 two orders of magnitude smaller than typical differences observed between simulations
244 using different models in the MISOMIP [Asay-Davis et al , 2016]. The similarity of the
245 Lagrangian and Eulerian simulations are also reflected in the fact that the simulations
246 have very similar ice-shelf melt rates and ocean temperature/salinity profiles (shown in
247 Figures S1 and Figures S2 in the supplementary materials).

248 The agreement between the Eulerian and Lagrangian simulations is a confirmation that
249 the Lagrangian model is able to simulate sub-ice-shelf cavities as well as the Eulerian
250 model does. This is a good starting point for moving beyond the capabilities of the
251 Eulerian model.

5. Iceberg calving experiment

252 The infrequency of large calving events together with the difficulty of placing observa-
253 tional instruments around tabular icebergs means that little is known about how calving
254 icebergs affect ocean circulation around the iceberg and at the ice front. The Lagrangian
255 ice-shelf model developed in this study allows us for the first time to simulate an iceberg
256 calving away from the ice shelf, and to study what effect this has on the ocean around the
257 iceberg and beneath the ice shelf. Since the Lagrangian iceberg/ice shelf model is fully
258 coupled to the ocean, the iceberg motion affects the ocean hydrography, and the changing
259 ocean conditions feedback onto the ice.

260 In this section, the Lagrangian ice shelf model is used to simulate a tabular iceberg
261 detaching from the ice shelf, and drifting into the open ocean. The results below show
262 that the calving of a large tabular iceberg can cause significant changes to the ocean
263 stratification and circulation around the iceberg and at the ice shelf front.

5.1. Setup of iceberg calving experiment:

264 The iceberg calving experiment is initialized using the final state of the static Lagrangian
265 ice shelf simulation (i.e.: at time $t = 10$ years). When initializing the calving event, we
266 bypass the question of how to prescribe a physical calving law [Benn et all , 2007; Alley
267 et al , 2008; Levermann et al , 2012; Bassis and Jacobs , 2013] by manually breaking off

268 a semi-circular iceberg. All ice elements initially within a 14.4 km radius of the center
269 of the ice front are allowed to move freely while the other ice elements continue to be
270 held stationary. Ice elements less than 12 km from the center of the ice front, are bonded
271 together to form a semi-circular tabular iceberg. A ring of elements whose distance, d ,
272 from the ice front center obeys $12 \text{ km} \leq d \leq 14.4 \text{ km}$, are allowed to move freely, but
273 have all their bonds removed.

5.2. Results of iceberg calving experiment

274 5.2.1. Ocean response to iceberg detachment

275 Immediately after the numerical bonds are broken, a large semi-circular tabular iceberg
276 detaches from the ice shelf, and begins to drift northwards (Figure 2). The northwards
277 motion of the iceberg creates a region of open water at the new calving front, between
278 the ice shelf and the tabular iceberg. The formation of a region of open ocean behind the
279 iceberg causes a sudden stretching of the water column in the wake of the iceberg, which
280 drives an upwelling throughout the water column. The negative background temperature
281 gradient (cold over warm) means that this upwelling is observed as warm water anomaly
282 beneath newly formed ice front (Figure 5a and 6a). The warming is observed through-
283 out the water column, but is largest near the surface. Similarly, the upwelling leads to
284 increased salinity beneath newly formed ice front (not shown).

285 The calving event also drives an immediate change in circulation around the newly
286 created ice front as the ocean adjusts to the topographic changes. Since the Coriolis
287 parameter is negative, a stretching of the water column behind the iceberg has to be
288 accompanied by the creation of negative relative vorticity in order for potential vorticity
289 (PV) to be conserved. The creation of negative relative vorticity along the newly calved

290 ice front, gives rise to a pair of oppositely orientated ocean jets running along the ice
291 front. A westward barotropic jet is created to the south of the calving front, and an
292 eastward barotropic jet is created to the north of the calving front (Figures 7a and 8b).
293 The positive gradient in zonal velocity created by this pair of oppositely orientated jets
294 yields the negative relative vorticity, needed to conserve PV.

295 To the north of the iceberg, the iceberg detachment has the opposite effect on the ocean.
296 The forward movement of the iceberg causes a squeezing of the water column directly in
297 front of the iceberg. This shortening of the water column causes a downwelling in the
298 water column in front of the iceberg, which is observed as a cool water anomaly in front
299 of the iceberg (Figure 5a). The squeezing of the water column generates positive relative
300 vorticity, so that the total PV is conserved. The positive relative vorticity creates an
301 eastward and westward jet to the south and north of the northern edge of the iceberg
302 (Figures 7a and 8b). The stretching and squeezing of the water column to the south and
303 north of the iceberg, both contribute to the eastward jet which forms directly beneath the
304 iceberg which plays an important role in driving iceberg motion.

305 (If you have time, check whether when the wind goes in the other direction, the jet
306 beneath the iceberg moves in the other direction.)

307 5.2.2. Iceberg motion

308 After the iceberg breaks away from the ice shelf, the motion of iceberg is primarily
309 driven by the drag from ocean currents beneath the iceberg, wind drag and by Coriolis
310 force. The eastward jet beneath the iceberg drives the iceberg towards the east (Figures
311 7a and 8b), while the wind and Coriolis force drive the iceberg offshore. Initially, as the
312 iceberg drifts eastward, it collides with the ice shelf, which hinders its motion (Figure 2a).

³¹³ Only once the iceberg has drifted sufficiently far northwards to be clear of the ice shelf,
³¹⁴ does it begin to drift towards the east. Once this happens, the iceberg velocity quickly
³¹⁵ adjusts so that it is approximately equal to the ocean velocity below the iceberg. As the
³¹⁶ iceberg drifts northwards, it rotates in a counter-clockwise direction (Figure 2).

³¹⁷ The motion of the iceberg plays a large role in setting the direction of the ocean flow
³¹⁸ below and around the iceberg, since the ocean has to adjust to topographical changes so
³¹⁹ that PV is conserved. This is illustrated, for example, by the change in orientation of
³²⁰ the ocean jets running beneath the iceberg that occurs as the iceberg rotates (Figure 7b).

³²¹ An important consequence of the controlling effect of iceberg topography is formation of
³²² a Taylor Column below the iceberg: the water column below the iceberg is constrained
³²³ to move at the same speed as the iceberg above, since differential motion would force
³²⁴ the water column out from under the iceberg, causing the water column to stretch, and
³²⁵ generating PV. This means that the column of water beneath the iceberg is largely sep-
³²⁶ arated from the water around the iceberg and strong gradients in temperature, salinity
³²⁷ and velocity can exist at the iceberg edge. In our experiment, a Taylor Column is clearly
³²⁸ observed below the iceberg throughout the simulation (Figure 9).

³²⁹ Once the iceberg reaches the eastern side of the domain, it begins to interact the bound-
³³⁰ ary of the domain and with the southward boundary current running along the edge of
³³¹ the domain (Figures 2b and 10c). The presence of the iceberg along the eastern boundary
³³² impedes the southward boundary current, so that the current has to flow to the west of
³³³ the iceberg (Figure 10b). The diverted current follows the topographic contour created by
³³⁴ the iceberg so that it sets up a counter-clockwise circulation running around the iceberg
³³⁵ (Figure 7c). The eastward jet which was previously positioned beneath the iceberg shifts

336 to the south and becomes part of the flow directing the boundary current around the ice-
337 berg. This counter-clockwise circulation around the iceberg remains around the iceberg
338 until the end of the simulation. Interestingly, the iceberg continues to move northward de-
339 spite the fact that it is moving within a southward flowing boundary current (Figure 9b).
340 This is partly due to the Taylor Column beneath the iceberg, which allows the northward
341 velocity beneath the iceberg to be separated from the southward moving current around
342 the iceberg.

343 **5.2.3. Surface warming and sub-surface cooling**

344 After the tabular iceberg detaches from the ice shelf, a warming is observed throughout
345 the water column to the south of the iceberg (Figure 5a, as discussed above). This warming
346 extends to the ocean surface, resulting in warm sea surface temperature (SST) anomalies
347 at the newly calved ice front and around the southern side of the iceberg (Figure 2 and
348 6a - make sure it is clear in the Figure). In the weeks following calving, part of this warm
349 SST anomaly remains at the ice front, influencing the heat flux into the ice shelf cavity,
350 and some the SST anomaly drifts with the iceberg into the open ocean.

351 The warm SST anomalies at the ice front persist and strengthen, even once the tabular
352 iceberg has drifted away, as water continues to upwell at the newly formed ice front. Some
353 of this warmed surface water is advected to west by the westward jet at the ice front (Figure
354 2c). Once these warmed surface waters reach the western side of the domain, most of this
355 warm anomaly is advected northwards following the western boundary, while some of the
356 warmth is forced southward, and is able to subduct beneath ice shelf on the western side
357 of the ice shelf front.

358 The SST anomalies that drift along with the iceberg are initially concentrated along
359 the curved southern side of the iceberg. As the tabular iceberg drifts away from the ice
360 shelf (and begins to rotate), the currents that develop around the iceberg advect this
361 warm SST anomaly counter-clockwise around the perimeter of the iceberg so that by 15
362 days after calving, the SST around the most of the iceberg's perimeter is anomalously
363 warm (Figure 2). As the iceberg drifts further into the open ocean, the warmed surface
364 waters around the iceberg's perimeter mix with the ambient surface water, leaving a trail
365 of warmed surface water which maps out the wake of the iceberg. It is likely that as
366 the iceberg drifts, the motion of the iceberg and strong sheer in horizontal velocity at
367 the iceberg edges contribute to continued upwelling, leading to further increased surface
368 warming.

369 As discussed above, the downwelling on the northern side of the iceberg observed im-
370 mediately after calving, leads to a cooling/freshening of the water column beneath and to
371 the north of the iceberg (Figure 5 and 6). As the iceberg drifts away from the ice shelf,
372 the cool water anomalies remain beneath the iceberg, traveling with the iceberg into the
373 open ocean, leaving a trail of cool subsurface temperature anomalies which maps out the
374 (subsurface) wake of the iceberg (not shown). The pattern of warm surface anomalies
375 around the iceberg, and cool subsurface anomalies around the iceberg, is clearly visible
376 throughout the simulation (Figure 9c), and suggests continued vertical mixing around the
377 iceberg perimeter as it drifts into the open ocean.

378 About 5 days after calving, as the iceberg begins to rotate counter clockwise, the jet
379 to the north of the iceberg begins to drive the cool water anomaly towards the ice front
380 (Figure 7b). The strong jet moving towards the ice front causes water to subduct beneath

381 the ice front, leading to further cool sub-surface anomalies. Below the depth of the
382 ice shelf, the cool water anomalies are stronger than the warm water anomalies caused
383 by the initial water column stretching. The subsurface negative temperature anomalies
384 strengthen over time and within a month of the calving event, the negative anomalies
385 occupy most of the water column close to the ice front (Figure 6). This subsurface cooling
386 at the ice front is the most prominent temperature response observed in our iceberg calving
387 experiments. Similar subsurface cooling at the ice front was observed in other experiments
388 using different sizes and shapes for the calving iceberg (not shown).

389 The zonal current along the ice front drives the cool anomaly to the west, causing an
390 enhancement of the cool anomalies on the western side of the ice shelf front (Figure 6c).
391 Most of the subsurface cooling occurs outside of the ice shelf cavity, as the dynamical
392 barrier caused by the ice shelf inhibits exchange of water across the ice front. However
393 over time, an increasing amount of cooler water is able to enter the ice shelf cavity, and
394 is advected below the ice shelf (Figure 5c).

395 **The sub-subsurface cooling and warm surface temperature anomalies discussed above**
396 **are accompanied by a freshening at depth and increase in surface salinity (not shown).**

397

398 **5.2.4. Inside the ice shelf cavity**

399 The combination of cool sub-surface temperature anomalies and elevated ocean veloci-
400 ties at the ice front, results in a temperature flux across the ice front, as cool temperature
401 anomalies to enter the ice shelf cavity (Figure 5). Once the cooler water has entered the
402 ice shelf cavity, the anomalies spread southwards within the ice shelf cavity, eventually
403 reaching all the way to the grounding line. As the cool water spreads into the cavity, it

⁴⁰⁴ mixes with the water within the ice shelf cavity, causing a reduction in the strength of
⁴⁰⁵ the anomaly towards the grounding line (Figure 5c).

⁴⁰⁶ The cooling of the water inside the ice shelf cavity after calving leads to a reduction of
⁴⁰⁷ the melt rates at the base of the ice shelf (Figure 11). The reduced melt rates occur over
⁴⁰⁸ a wide area extending from the newly calved ice front, all the way towards the grounding
⁴⁰⁹ line. The negative melt rate anomalies increase over time, as more cold water enters the
⁴¹⁰ ice shelf cavity. The strongest negative anomalies are observed near the ice front, while
⁴¹¹ the strength of the negative melt rate anomalies are reduced towards the grounding. The
⁴¹² reduction in melt rates are up to 0.5 m per year, which is small compared to the mean
⁴¹³ melt rates near the grounding line, but is a substantial fraction of the melt at intermediate
⁴¹⁴ depths (Figure S4a).

⁴¹⁵ Near the ice front, the competing effects of warm surface water subducting beneath the
⁴¹⁶ ice shelf on the flanks of the domain, and the cool water entering the ice shelf in the enter
⁴¹⁷ of the domain, lead to a complex of pattern of positive and negative melt rate anomalies
⁴¹⁸ within 20 km of the ice front (Figure S4).

⁴¹⁹ 5.2.5. Equilibrium hydrography

⁴²⁰ The presence of a northern boundary in our simulation mean that we are unable to
⁴²¹ entirely remove the iceberg from the domain and observe the system approaching a new
⁴²² equilibrium state. However, a comparison between the iceberg calving simulation and an
⁴²³ ‘equilibrium-shelf simulation’ (where the model was spun up with the iceberg removed
⁴²⁴ from the start), shows that after 60 days the hydrography inside the ice shelf cavity
⁴²⁵ in the iceberg-calving simulation appears to be qualitatively similar to equilibrium-shelf
⁴²⁶ simulation steady state (see Figure S5 in the supplementary material, for example). This

⁴²⁷ suggests that the processes occurring at the ice front directly after calving are transient
⁴²⁸ processes which allow the system to move towards a steady state that is largely controlled
⁴²⁹ by the ice shelf geometry. Since the ice shelf geometry in our simulation is highly idealized
⁴³⁰ and is in a closed domain, it is unclear whether the adjustment time scale seen here is
⁴³¹ relevant to real-world ice shelves.

6. Conclusion

⁴³² This study presents a new Lagrangian framework for modeling sub-ice-shelf cavities. In
⁴³³ this framework, the ice shelf is constructed out of many Lagrangian elements, which are
⁴³⁴ bonded together by numerical bonds. By breaking the bonds, we can use the Lagrangian
⁴³⁵ model to simulate iceberg calving, and to observed the ocean response to large calving
⁴³⁶ events (Figures 2). This capability is currently not possible using more traditional Eulerian
⁴³⁷ models [Stern et al , 2017].

⁴³⁸ We validate the Lagrangian ice shelf model by simulating the flow beneath a (static)
⁴³⁹ idealized ice shelf, and comparing the results to an existing Eulerian model simulation
⁴⁴⁰ with identical configuration. This comparison show that the results from Lagrangian
⁴⁴¹ and Eularian models are almost indistinguishable. This agreement confirms that the
⁴⁴² Lagrangian model is able to simulate sub-ice-shelf cavities as well as the Eulerian model.
⁴⁴³ Demonstrating that the Lagrangian ice-shelf model is able to reproduce the results of
⁴⁴⁴ an Eulerian ice-shelf model in the same static ice-shelf configuration is a prerequisite
⁴⁴⁵ developing more advanced Lagrangian models and represents a good benchmark test for
⁴⁴⁶ new Lagrangian ice-shelf models.

⁴⁴⁷ The Lagrangian model is then used to simulate a semi-circular iceberg detaching from
⁴⁴⁸ the ice shelf. The results demonstrate that the calving of a large tabular iceberg can cause

449 significant changes to the ocean stratification and circulation around the iceberg and at
450 the ice front. A number of robust features were observe in this iceberg-calving simulation,
451 which could have real-world analogues:

452 • As the iceberg detaches from the ice shelf, there is an immediate dynamical ocean
453 response: a stretching of the water column directly behind the iceberg gives rise to ocean
454 upwelling, which leads to a warm salty anomalies being created at the newly calved
455 ice front. PV conservation implies that this ocean column stretching gives rise to the
456 formation for pair of oppositely orientated jets which form directly behind berg. A similar
457 (and oppositely signed) phenomenon occurs in front of the berg, where a squeezing of the
458 water column leads to downwelling, a cooling/freshening of the water column and a pair
459 of oppositely orientated jets being created along the front side of the iceberg.

460 • The iceberg topography has a controlling affect on the ocean below it. This is demon-
461 strated by the shifting of ocean jets below the iceberg in response to the iceberg motion. It
462 is also demonstrated by the Taylor forms directly below the iceberg. This Taylor column
463 follows the iceberg as it drifts into the open ocean and leads to a separation between the
464 ocean properties below the iceberg and the ambient ocean conditions.

465 • The calving and motion of the iceberg has a large and complex affect on ocean
466 temperate and salinity around the iceberg and at the calving front. In our experiment,
467 warmed water surrounds the iceberg as it drift away from the ice shelf and maps out
468 a trail of warm surface anomalies in the wake of the iceberg. Similarly, cooler waters
469 are observed below the iceberg and map out a trail of cool sub-surface anomalies in the
470 iceberg wake.

471 ● As the iceberg drifts away from the ice shelf, it interacts with the ocean current
472 coming towards the ice shelf. The iceberg impedes the ocean current which is diverted
473 around the iceberg and sets up a new circulation around the iceberg. In our simulation,
474 the change in circulation directs a current towards the center of the ice shelf front. This
475 water subduct causing large cool anomalies at the ice front.

476 ● Large changes in ocean properties which occur at the ice front following the iceberg
477 calving can directly affect the temperature flux into the ice shelf cavity, which in turn
478 alter the sub-ice shelf melt rates. In our experiment, the cool water subducting beneath
479 the ice shelf lead to reduced melt rates beneath the ice shelf. This decrease in melt rate
480 extends far into the ice shelf cavity.

481 ● Once the iceberg has drifted far away from the ice shelf cavity, the conditions and
482 melt rates within the ice-shelf cavity appear to be converge towards values similar to those
483 in simulations run with the iceberg removed from the start. This result suggests that the
484 melt rates inside the ice shelf cavity are largely controlled by the ice shelf geometry.
485 The changes in ocean conditions caused by the interaction with the iceberg appear to be
486 transient adjustment processes.

487 The results from this experiment demonstrate the complex interaction between a calv-
488 ing iceberg and the surrounding ocean, and suggests that iceberg-ocean interactions can
489 significantly affect ocean currents and hydrography around calving sites, and can even
490 feedback onto melt rates within the ice shelf cavity. More work is needed to further un-
491 derstand these iceberg-ocean interactions, and to gauge how these dynamics might affect
492 real-world ice shelf cavities. The Lagrangian ice shelf model presented in this study could
493 be a useful tool to study these interactions using both idealized and real-world geometries.

References

- 494 Asay-Davis, X. S., S. L. Cornford, B. K. Galton-Fenzi, R. M. Gladstone, G. H. Gudmundsson, D. M. Holland, P. R. Holland, and D. F. Martin (2016), Experimental design for
495 three interrelated marine ice sheet and ocean model intercomparison projects: MIS-
496 MIP v. 3 (MISMIP+), ISOMIP v. 2 (ISOMIP+) and MISOMIP v. 1 (MISOMIP1).
497 *Geoscientific Model Development* 9, no. 7: 2471.
- 498 Arrigo, K. R., G. L. van Dijken, D. G. Ainley, M. A. Fahnestock, and T. Markus (2002).
499 Ecological impact of a large Antarctic iceberg. *Geophys. Res. Lett.*, 29(7).
- 500 Alley, R. B., H. J. Horgan, I. Joughin, K. M. Cuffey, T. K. Dupont, B. R. Parizek, S.
501 Anandakrishnan, and J. Bassis (2008), A simple law for ice-shelf calving. *Science* 322,
502 no. 5906, 1344-1344.
- 503 Bassis, J. N., and S. Jacobs (2013), Diverse calving patterns linked to glacier geometry.
504 *Nature Geoscience*, 6(10), 833-836.
- 505 Benn, D. I., C. R. Warren, and R. H. Mottram (2007). Calving processes and the dynamics
506 of calving glaciers. *Earth-Science Reviews*, 82(3), 143-179.
- 507 Bigg, G. R., Wadley, M. R., Stevens, D. P., and Johnson, J. A. (1997), Modeling the
508 dynamics and thermodynamics of icebergs. *Cold Regions Science and Technology*, 26(2),
509 113-135.
- 510 Borstad, C. P., A. Khazendar, E. Larour, M. Morlighem, E. Rignot, M. P. Schodlok, and
511 H. Seroussi (2012), A damage mechanics assessment of the Larsen B ice shelf prior to
512 collapse: Toward a physically-based calving law, *Geophys. Res. Lett.*, 39, L18502
- 513 Biddle, L. C., J. Kaiser, K. J. Heywood, A. F. Thompson and A. Jenkins (2015), Ocean
514 glider observations of iceberg-enhanced biological productivity in the northwestern Wed-
- 515

- 516 dell Sea, *Geophys. Res. Lett.*, 42, 459465.
- 517 De Rydt, J., and G. H. Gudmundsson (2016), Coupled ice shelf ocean modeling and
518 complex grounding line retreat from a seabed ridge. *J. of Geophys. Res.: Earth Surface*,
519 121(5), 865-880.
- 520 Dunne, J.P., J.G. John,, A.J. Adcroft, S.M. Griffies, R.W. Hallberg, E. Shevliakova,
521 R.J. Stouffer, W. Cooke, K.A. Dunne, M.J Harrison, and J.P. Krasting (2012), GFDL's
522 ESM2 global coupled climate-carbon Earth System Models. Part I: Physical formulation
523 and baseline simulation characteristics. *J. of Climate*, 25(19), 6646-6665.
- 524 Depoorter, M. A., J. L. Bamber, J. A. Griggs, J. T. M. Lenaerts, Stefan RM Ligtenberg,
525 M. R. van den Broeke, and G. Moholdt (2013), Calving fluxes and basal melt rates of
526 Antarctic ice shelves. *Nature*, 502(7469), 89-92.
- 527 Determan J., Gerdes R. (1994), Melting and freezing beneath ice shelves: implications
528 from a three-dimensional ocean-circulation model. *Ann. Glaciol.*, 20, 413-419.
- 529 Dowdeswell, J. A., and J. L. Bamber (2007), Keel depths of modern Antarctic icebergs
530 and implications for sea-floor scouring in the geological record. *Marine Geology*, 243(1),
531 120-131.
- 532 Duprat, L. P., G. R. Bigg, and D. J. Wilton (2016), Enhanced Southern Ocean marine
533 productivity due to fertilization by giant icebergs. *Nature Geoscience*.
- 534 Eckert, E. R. G. (1950). Introduction to the Transfer of Heat and Mass. McGraw-Hill.
- 535 Gladstone, R. M., G. R. Bigg, and K. W. Nicholls. (2001), Iceberg trajectory modeling
536 and meltwater injection in the Southern Ocean (19782012). *J. of Geophys. Res.: Oceans*,
537 106(C9), 19903-19915.

- 538 Goldberg, D. N., C. M. Little, O. V. Sergienko, A. Gnanadesikan, R. Hallberg, and M.
539 Oppenheimer (2012), Investigation of land ice?ocean interaction with a fully coupled
540 ice-ocean model: 1. Model description and behavior. *J. of Geophys. Res.: Earth Surface*,
541 117(F2).
- 542 Gladish, C. V., D. M. Holland, P. R. Holland, and S. F. Price (2012), Ice-shelf basal
543 channels in a coupled ice/ocean model. *J. of Glaciol.*, 58(212), 1227-1244.
- 544 Grosfeld K., R. Gerdes, J. Determan (1997), Thermohaline circulation and interaction
545 between ice shelf cavities and the adjacent open ocean. *J. Phys. Oceanogr.*, **102**, C7,
546 15959-15610.
- 547 Grosfeld, K., and H. Sandhger, (2004). The evolution of a coupled ice shelfocean system
548 under different climate states. *Global and Planetary Change*, 42(1), 107-132.
- 549 Hallberg, R., A. Adcroft, J. P. Dunne, J. P., Krasting, R. J., and Stouffer (2013), Sensitiv-
550 ity of twenty-first-century global-mean steric sea level rise to ocean model formulation.
551 *J. of Climate*, 26(9), 2947-2956.
- 552 Holland D. M., Jenkins A. (2001), Adaptation of an isopycnic coordinate ocean model for
553 the study of circulation beneath ice shelves. *Mon. Wea. Rev.*, 129, 1905-1927.
- 554 Holland P. R. and D. L. Feltham (2006), The effects of rotation and ice shelf topography
555 on frazil-laden Ice Shelf Water plumes. *J. Phys. Oceanogr.*, 36, 2312-2327.
- 556 Holland, D. M., and A. Jenkins (1999), Modeling thermodynamic ice-ocean interactions
557 at the base of an ice shelf. *J. of Phys. Oceanogr.* 29.8, 1787-1800.
- 558 Hellmer H.H., Olbers D. J. (1989), A two-dimensional model for the thermohaline circu-
559 lation under an ice shelf. *Antarctic Science*, 1, 325- 336.

- 560 Hopkins, M. A. (1996). On the mesoscale interaction of lead ice and floes. *J. of Geophys. Res.: Oceans*, 101(C8), 18315-18326.
- 562 Jakobsen, T. (2001). Advanced character physics. In *Game Developers Conference*, Vol. 3.
- 564 Jenkins, A., P. Dutrieux, S. S. Jacobs, S. D. McPhail, J. R. Perrett, A. T. Webb, and
565 D. White (2010), Observations beneath Pine Island Glacier in West Antarctica and
566 implications for its retreat. *it Nature Geo.*, 3(7), 468-472.
- 567 Jacobs, S. S., A. Jenkins, C. F. Giulivi, and P. Dutrieux (2011). Stronger ocean circulation
568 and increased melting under Pine Island Glacier ice shelf. *Nature Geo.*, 4(8), 519-523.
- 569 Jongma, J. I., E. Driesschaert, T. Fichefet, H. Goosse, and H. Renssen (2009), The effect of
570 dynamic-thermodynamic icebergs on the Southern Ocean climate in a three-dimensional
571 model, *Ocean Modell.*, 26, 104113.
- 572 Lewis E.L. and R.G. Perkin (1986), Ice pumps and their rates. *J. of Geophys. Res.*, 91,
573 11756-11762.
- 574 Losch, M. (2008). Modeling ice shelf cavities in az coordinate ocean general circulation
575 model. *J. of Geophys. Res.: Oceans*, 113(C8).
- 576 Li, B., H. Li, Y. Liu, A. Wang and S. Ji (2014), A modified discrete element model for
577 sea ice dynamics. *Acta Oceanologica Sinica*, 33(1), 56-63.
- 578 Liu, M. B. and G. R. Liu (2010), Smoothed particle hydrodynamics (SPH): an overview
579 and recent developments. *Archives of computational methods in engineering*, 17(1), 25-
580 76.
- 581 Lichy, C., and H. H. Hellmer (2001). Modeling giant-iceberg drift under the influence of
582 sea ice in the Weddell Sea, Antarctica. *J. of Glaciol.*, 47(158), 452-460.

- 583 Levermann, A., T. Albrecht, R. Winkelmann, M. A. Martin, M. Haseloff, and I. Joughin.
584 (2012), Kinematic first-order calving law implies potential for abrupt ice-shelf retreat.
585 *The Cryosphere*, 6(2), 273-286.
- 586 Martin, T., and Adcroft, A. (2010), Parameterizing the fresh-water flux from land ice
587 to ocean with interactive icebergs in a coupled climate model. *Ocean Modelling*, 34(3),
588 111-124.
- 589 Marsh, R., V. O. Ivchenko, N. Skliris, S. Alderson, G. R. Bigg, G. Madec, A. T. Blaker
590 Y. Aksenov, B. Sinha, A.C. Coward, and J.L. Sommer (2015), NEMOICB (v1. 0):
591 interactive icebergs in the NEMO ocean model globally configured at eddy-permitting
592 resolution. *Geoscientific Model Development* 8, no. 5 (2015): 1547-1562.
- 593 MacAyeal D.R. (1984), Thermohaline Circulation Below the Ross Ice Shelf: A Conse-
594 quence of Tidally Induced Vertical Mixing and Basal Melting. *J. Geophys. Res.*, 89,
595 597-606
- 596 Nicholls K.W. (1996), Temperature variability beneath Ronne Ice Shelf, Antarctica, from
597 thermistor cables. *J. Phys. Oceanogr.*, 11, 1199-1210.
- 598 Nicholls KW, Østerhus S, Makinson K (2009), Ice-Ocean processes over the continental
599 shelf of the southern Weddell Sea, Antarctica: a review. *Rev. Geophys.* 47(3).
- 600 Omelyan, I. P., M. I. Mryglod, and R. Folk (2002), Optimized Verlet-like algorithms for
601 molecular dynamics simulations. *Physical Review E*, 65(5), 056706.
- 602 Rignot, E., S. Jacobs, J. Mouginot, and B. Scheuchl (2013), Ice-shelf melting around
603 Antarctica. *Science*, 341, no. 6143 (2013): 266-270.
- 604 Robinson, N. J., and Williams, M. J. M. (2012). Iceberg-induced changes to polynya
605 operation and regional oceanography in the southern Ross Sea, Antarctica, from in situ

- 606 observations. *Antarctic Science*, 24(5), 514-526.
- 607 Pan, W., A. M. Tartakovsky, and J. J. Monaghan (2013). Smoothed particle hydrody-
608 namics non-Newtonian model for ice-sheet and ice-shelf dynamics. *J. of Comp. Phys.*,
609 242, 828-842.
- 610 Pralong, A., and M. Funk (2005), Dynamic damage model of crevasse opening and appli-
611 cation to glacier calving, *J. Geophys. Res.*, 110, B01309.
- 612 Seroussi H., Y. Nakayama, E.Y. Larour, D. Menemenlis, M. Morlighem, E. Rignot, and A.
613 Khazendar (2017), Continued retreat of Thwaites Glacier, West Antarctica, controlled
614 by bed topography and ocean circulation, *Geophys. Res. Lett.*, 44
- 615 Sergienko, O. V. (2013). Basal channels on ice shelves. *J. of Geophys. Res.: Earth Surface*,
616 118(3), 1342-1355.
- 617 Silva, T. A. M., Bigg, G. R., and Nicholls, K. W. (2006), Contribution of giant icebergs
618 to the Southern Ocean freshwater flux. *J. of Geophys. Res.: Oceans*, 111(C3).
- 619 Smith, K., B. Robison, J. Helly, R. Kaufmann, H. Ruhl, H., T. Shaw, and M. Vernet
620 (2007), Free-drifting icebergs: Hotspots of chemical and biological enrichment in the
621 Weddell Sea, *Science*, 317, 478482.
- 622 Stern, A. A., D. M. Holland, P. R. Holland, A. Jenkins and J. Sommeria (2014), The effect
623 of geometry on ice shelf ocean cavity ventilation: a laboratory experiment. *Experiments*
624 *in Fluids*, 55(5), 1-19.
- 625 Stern, A.A., Johnson, E., Holland, D.M., Wagner, T.J., Wadhams, P., Bates, R., Abra-
626 hamsen, E.P., Nicholls, K.W., Crawford, A., Gagnon, J. and Tremblay, J.E. (2015),
627 Wind-driven upwelling around grounded tabular icebergs. *J. of Geophys. Res.: Oceans*,
628 120(8), 5820-5835.

- 629 Stern, A. A., A. Adcroft, and O. Sergienko (2016), The effects of Antarctic iceberg calv-
630 ing?size distribution in a global climate model. *J. of Geophys. Res.: Oceans*, 121(8),
631 5773-5788.
- 632 Stern, A. A., A. Adcroft, O. Sergienko, G. Marques, R. Hallberg (2017), Modeling tabular
633 icebergs coupled to an ocean model. *Ocean Modeling*
- 634 Swope, W. C., H. C. Andersen, P. H. Berens, and K. R. Wilson (1982), A computer
635 simulation method for the calculation of equilibrium constants for the formation of
636 physical clusters of molecules: Application to small water clusters. *The Journal of
637 Chemical Physics* 76, no. 1, 637-649.
- 638 Tournadre, J., N. Bouhier, F. Girard-Ardhuin, and F. Rmy (2016), Antarctic icebergs
639 distributions 1992-2014. *J. Geophys Res: Oceans*.
- 640 Vernet, M., et al. (2012), Islands of ice: Influence of free-drifting Antarctic icebergs on
641 pelagic marine ecosystems, *Oceanography*, 25(3), 3839
- 642 Weeks, W. F., and W. J. Campbell (1973). Icebergs as a fresh-water source: an appraisal.
643 *J. of Glaciol.*, 12(65), 207-233.
- 644 White, L., A. Adcroft, and R. Hallberg (2009), High-order regriddingremapping schemes
645 for continuous isopycnal and generalized coordinates in ocean models. *J. of Comp.
646 Phys.*, 228(23), 8665-8692.

6.1. Supplementary material

647 This must be moved to its own document.

6.2. Static ice-shelf simulation

- 648 The results in the Lagrangian static ice-shelf simulation fit within the current under-
649 standing of ice-shelf cavity circulations based on ice-shelf observations [MacAyeal , 1984;

Lewis and Perkin , 1986; Jacobs et al , 2011] and previous modeling efforts [Determan and Gerdes , 1994; Holland and Feltham , 2006; Losch , 2008]. The ocean temperatures inside the domain are warmer than the in-situ freezing point (Figure S3a), and cause melting at the ice-shelf base (Figure S4a). The meltwater entering the domain is more buoyant than the water around it, and rises along the ice shelf as a cool fresh plume (Figure S3b,c). This injection of positive buoyancy at depth drives a clockwise circulation outside of the ice-shelf cavity (Figure 4a), providing the ice-shelf cavity with a continuous supply of warm water, which provides the thermal energy required for continuous ice-shelf melt. Strong meridional jets are observed at the ice front along the flanks of the domain, fluxing water into the ice shelf cavity on the eastern flank and allowing water to leave the ice shelf cavity on the western side (Figure 4a). The meridional flow in the center of the ice front is much smaller, consistent with the dynamical barrier at the ice shelf front discussed in previous modeling and experimental studies [Holland and Jenkins , 2001; Stern et al , 2014].

The highest melt rates are observed within 100km of the grounding line (Figure S4a). These elevated melt rates are caused by the presence of warm water (Figure S4b) and increased ocean velocities (Figure S4c) near the grounding line, as well as the fact that freezing point of ice decreases with increasing pressure. Elevated melt rates are also seen near the ice front, caused by strong currents running along the ice-shelf front (Figure S4c).

668

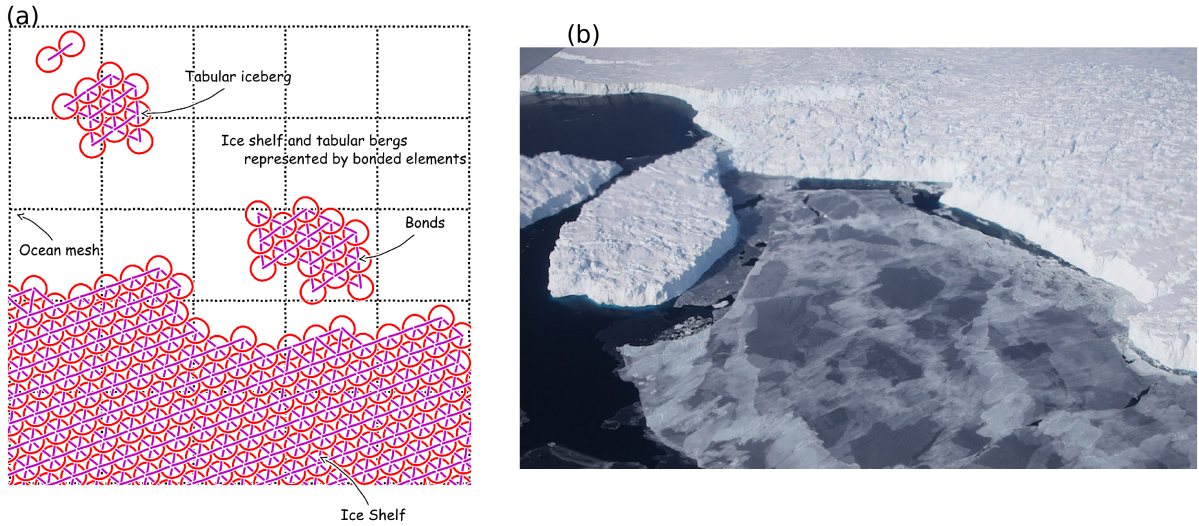


Figure 1. Schematic showing how ice shelves and tabular icebergs are constructed using Lagrangian elements. (a) Schematic of multiple ice elements that are joined together by numerical bonds (magenta lines) to form larger structures such as ice shelves and tabular icebergs. These numerical elements have finite extent and are able to interact with the ocean across multiple grid cells, and can interact with other elements. (b) Areal photograph of an ice shelf and tabular iceberg with elements superimposed over it to illustrate how the Lagrangian elements can be used to model ice shelves and tabular icebergs. In this schematic the ice elements (purple dots) are initialized in a staggered lattice covering the surface area of the iceberg. For purposes of mass aggregation, the ice elements are assumed to have hexagonal shape (red hexagons). For purposes of element interactions, the ice elements are assumed to be circular (black circles). Elements are initially bonded to adjacent elements using numerical bonds (magenta lines). These numerical bonds form equilateral triangles which give the shape rigidity. An ocean grid has been included (dashed cyan lines).

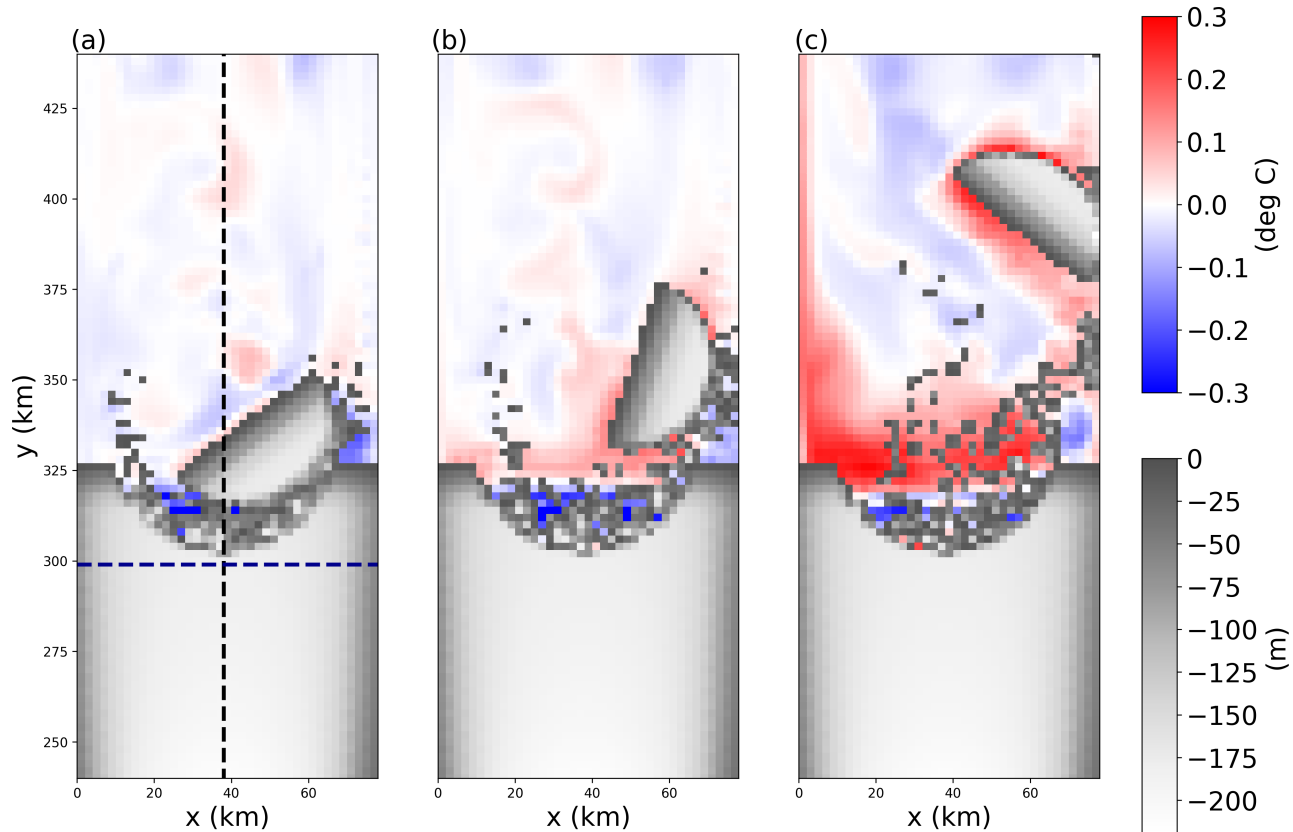


Figure 2. Snapshots of sea surface temperature anomalies in the iceberg calving simulation.

The anomalies are relative to pre-calving temperatures. Snapshots are taken (a) 7, (b) 15, and (c) 50 days after calving. Grid cells with ice mass $> 10^4$ kg are plotted in white, with grey shading indicating thinner ice. The black and blue dashed line in panel (a) shows the location of the vertical transects shown in Figures 5 and 6, respectively

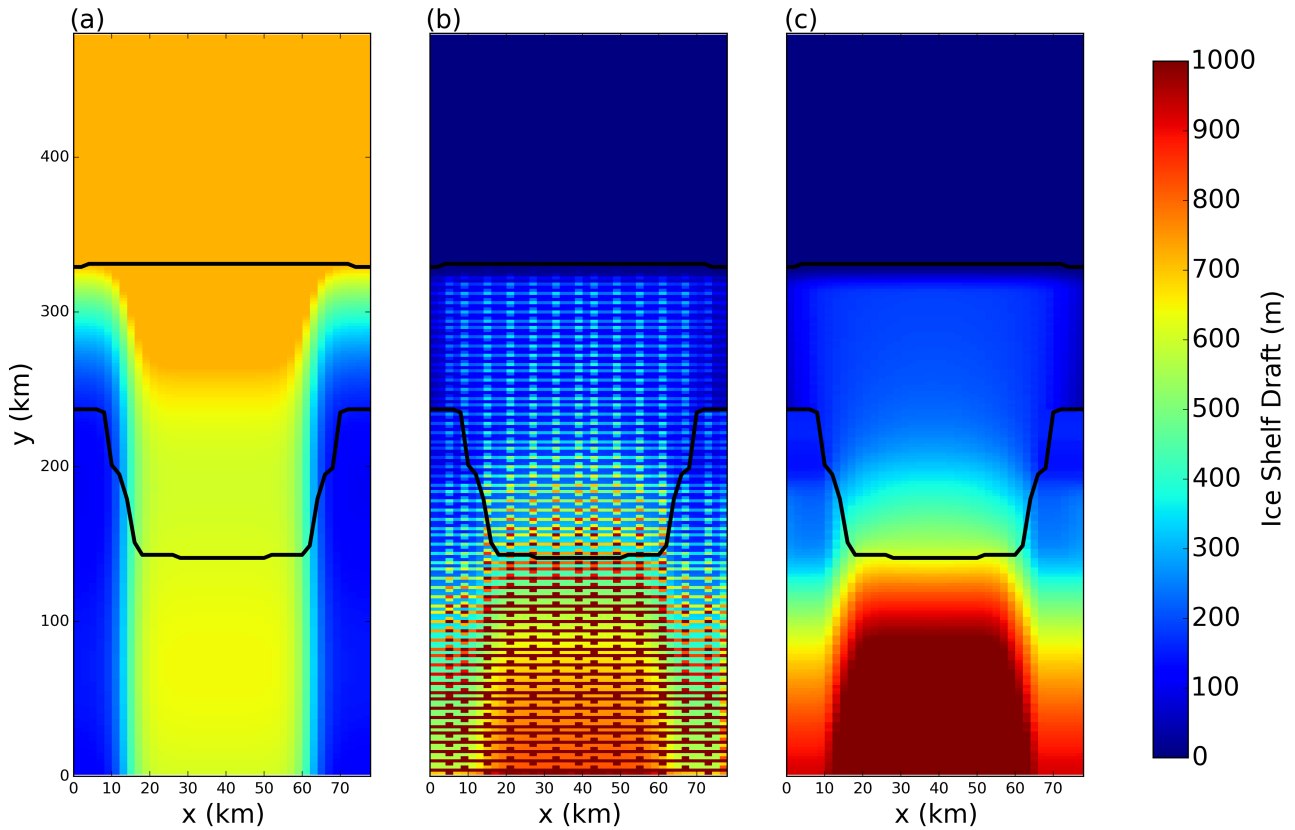


Figure 3. (a) Ocean bottom topography and (c) ice-shelf draft used to initialized the static ice shelf experiment simulation. The ice draft is calculated from the total mass in an ocean grid cell after the mass-spreading interpolation has been applied. Panel (b) shows the initial ice draft that would be calculated if the mass-spreading interpolation were not used (i.e. elements treated as point masses). The lower and upper black lines denote the grounding line and ice shelf front, respectively. This figure is reproduced from [Stern et al , 2017].

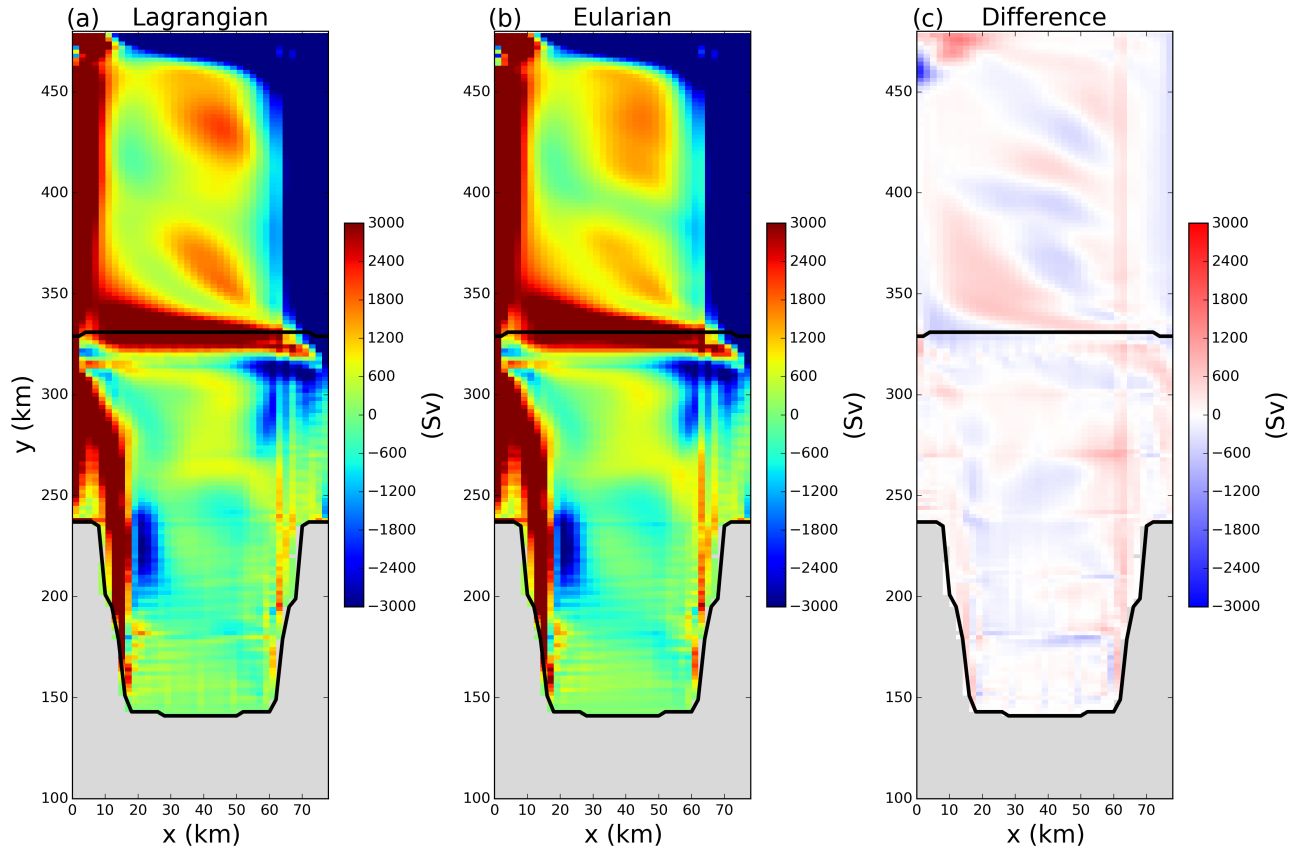


Figure 4. Time-averaged barotropic stream function in the (a) Lagrangian and (b) Eulerian simulations in the static ice-shelf configuration. Panel (c) shows the difference between panels (a) and (b). The time averages are taken over 5 years of model time, beginning at the end of the 5 year spin up period. **Something is wrong with the units in this figure**

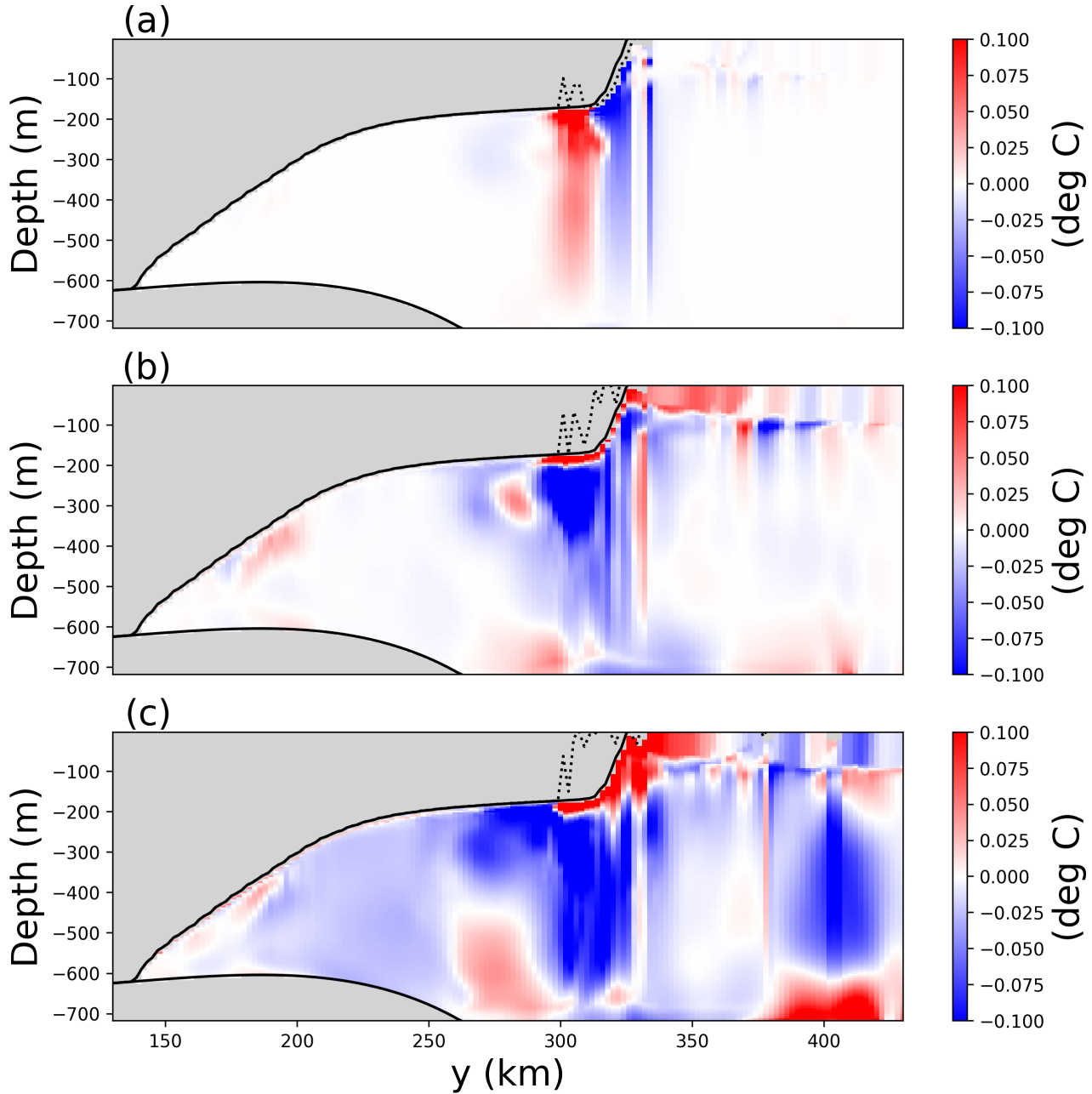


Figure 5. Snapshots of vertical sections of ocean temperature anomaly at $x=40$ km in the iceberg-calving experiment. The anomalies are relative to pre-calving temperatures. Snapshots are taken (a) 1, (b) 15, and (c) 50 days after calving. In each panel, the base of the ice before calving and at the time of the snapshot are shown by the solid and dashed black lines, respectively. Positions that were not the ocean interior at both snapshots are masked in grey. The position of the vertical transects is shown by the black dashed lines in Figure 2a.

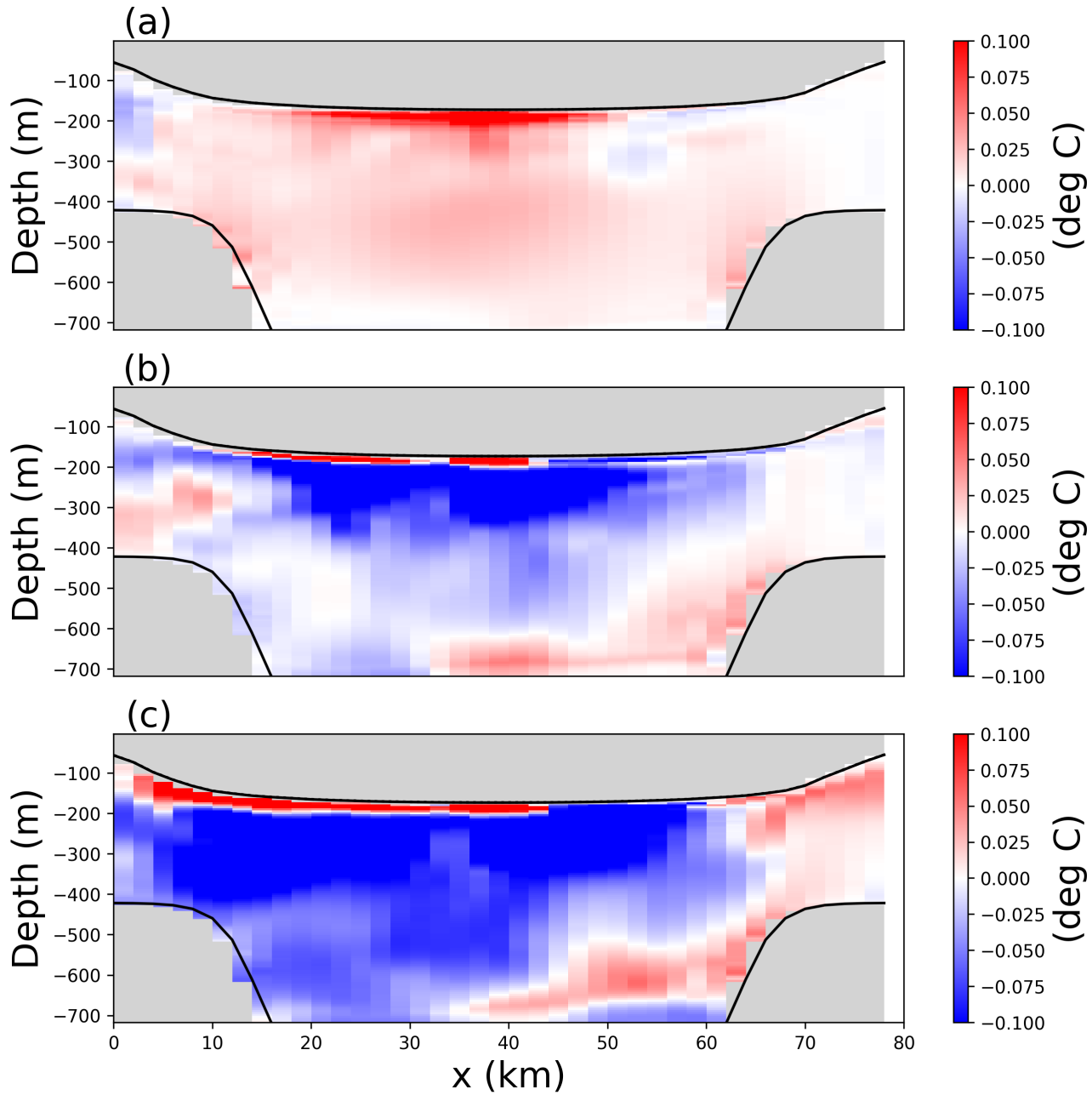


Figure 6. Snapshots of vertical sections of ocean temperature anomaly at $y = 300$ km in the tabular-iceberg-calving experiment. The anomalies are relative to pre-calving temperatures. Snapshots are taken (a) 1, (b) 15, and (c) 50 days after calving. The position of the vertical transects is shown by the blue dashed lines in Figure 2a. Should include the warming just after calving perhaps

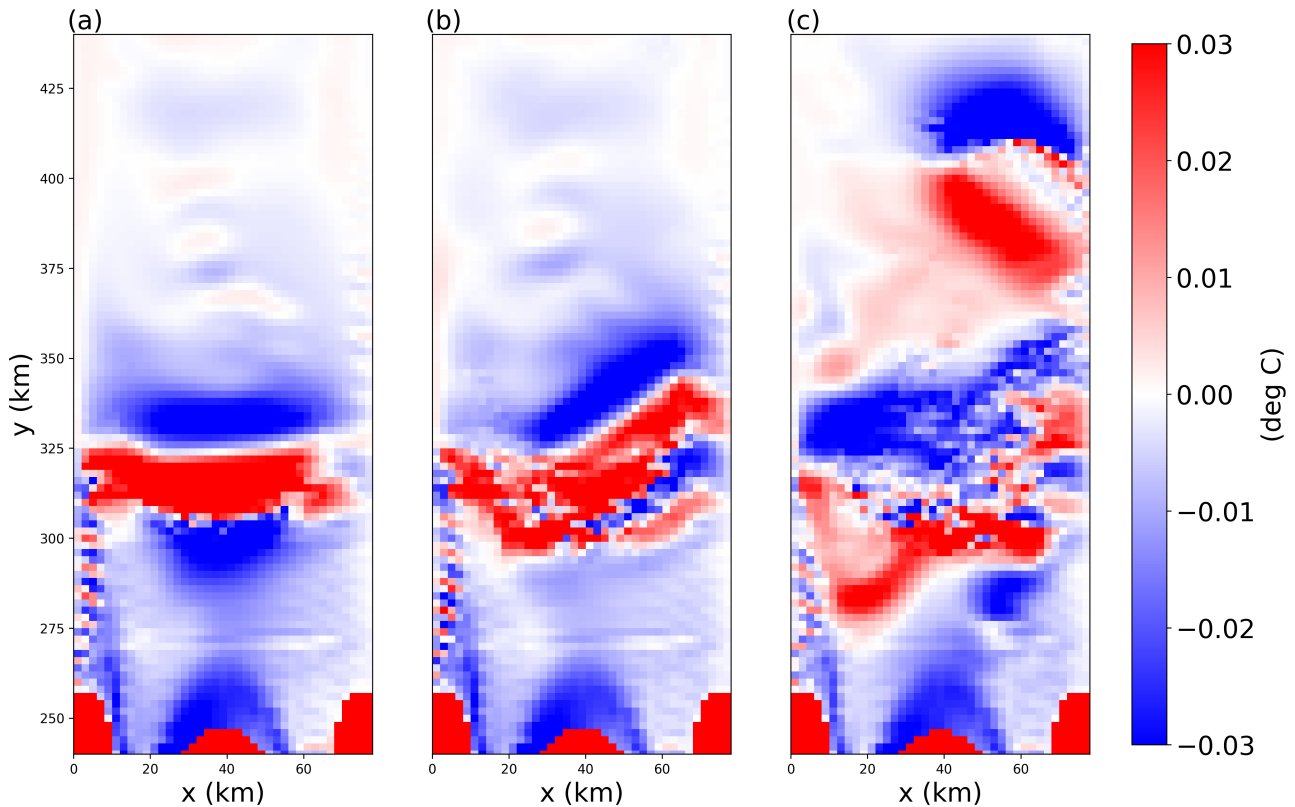


Figure 7. Snapshots of ocean zonal velocity at $z=197.5$ m(?) in the iceberg-calving experiment.

Snapshots are taken (a) 1, (b) 15, and (c) 50 days after calving. I should include an outline of the iceberg shape in this figure

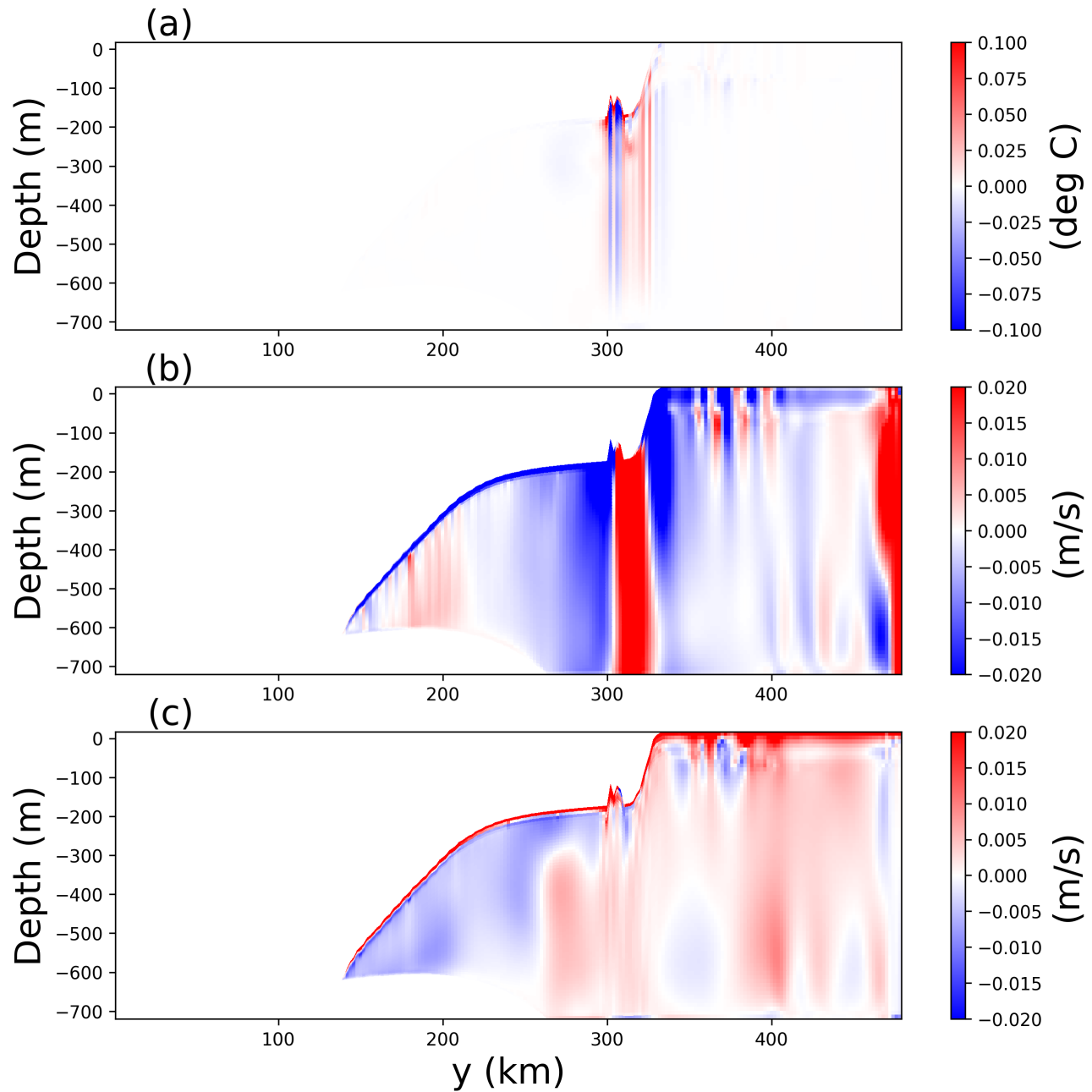


Figure 8. Panel b: Zonal velocity at ice front, 1 day after calving. **This figure still needs to be fixed**

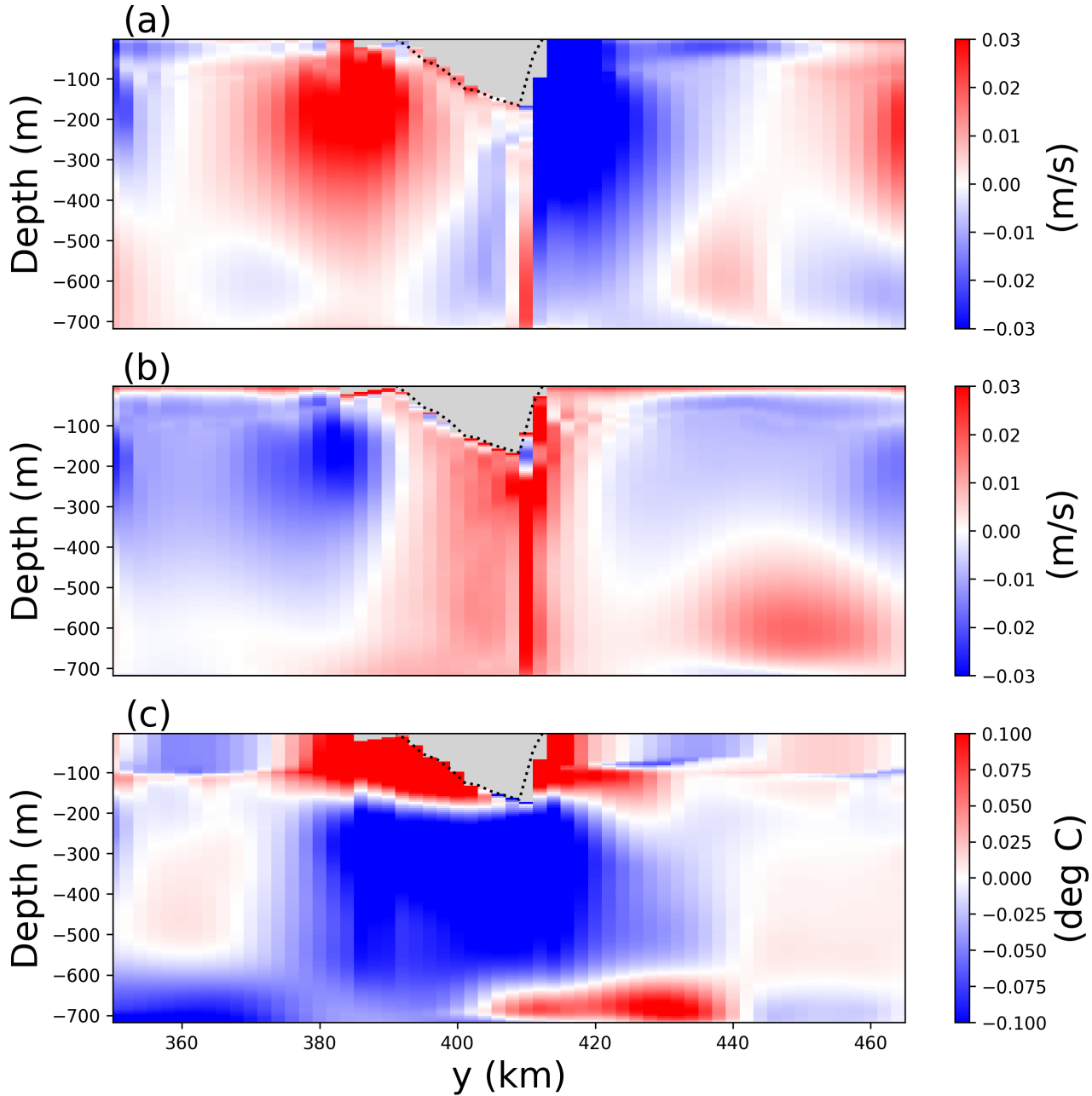


Figure 9. Snapshots of vertical sections of ocean (i) zonal velocity, (ii) meridional velocity, and (iii) temperature anomaly at $y=60$ km in the tabular-iceberg-calving experiment. The anomalies are relative to pre-calving temperatures. Snapshots are taken 50 days after calving. The position of the vertical transects is shown by the dashed lines in Figure 2c.

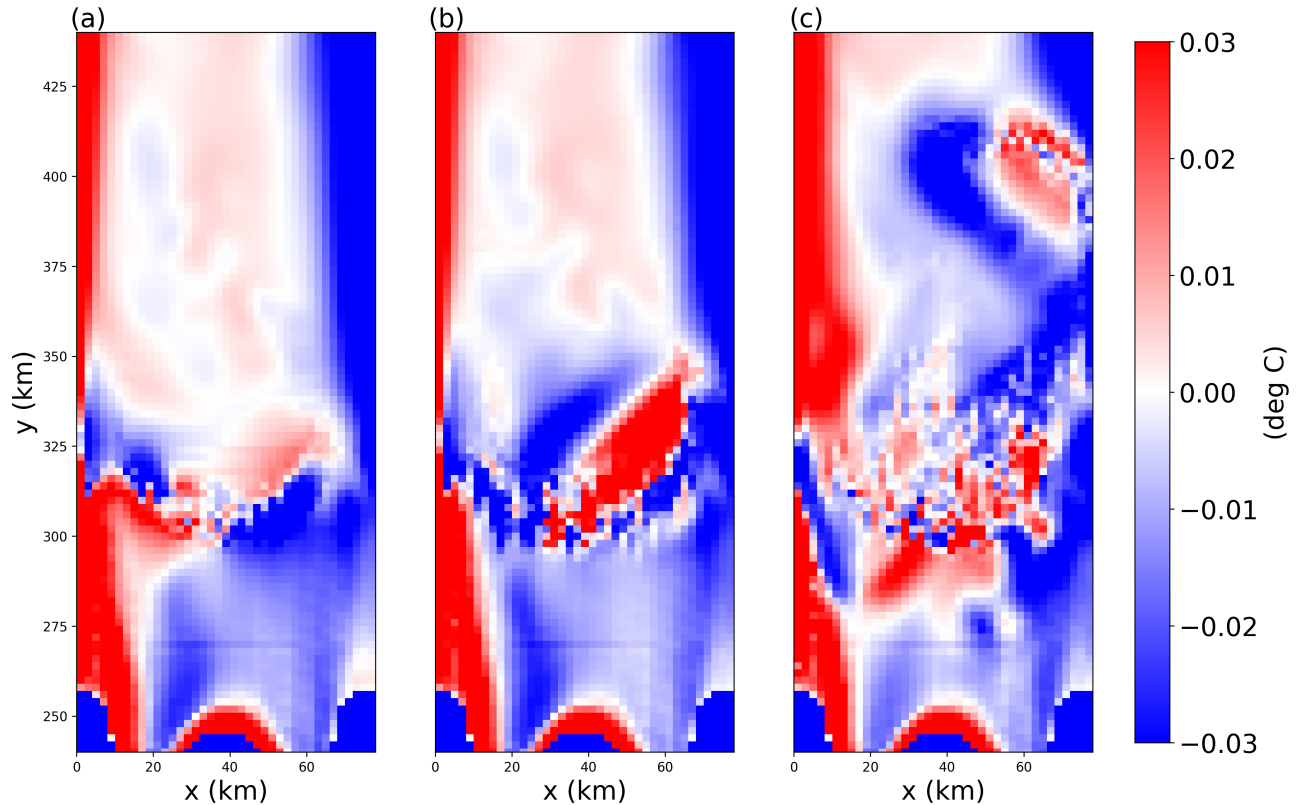


Figure 10. Snapshots of ocean meridional velocity at $z=197.5$ m in the iceberg-calving experiment. Snapshots are taken (a) 1, (b) 15, and (c) 50 days after calving. I should include an outline of the iceberg shape in this figure

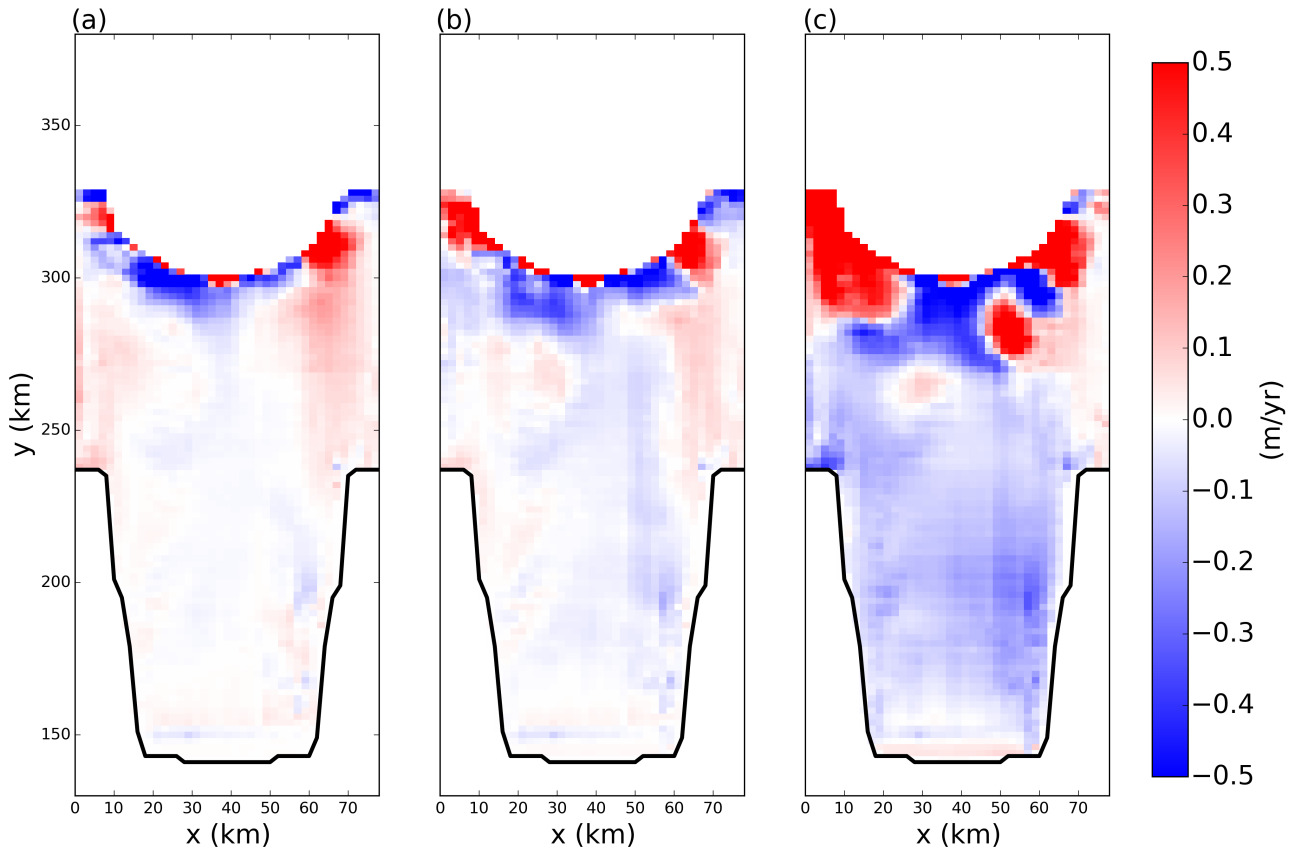


Figure 11. Snapshots of the melt rate anomaly, at the ice-shelf base in the tabular iceberg calving simulation. The anomalies are relative to pre-calving temperatures. Snapshots are taken (a) 7, (b) 15, and (c) 50 days after calving.

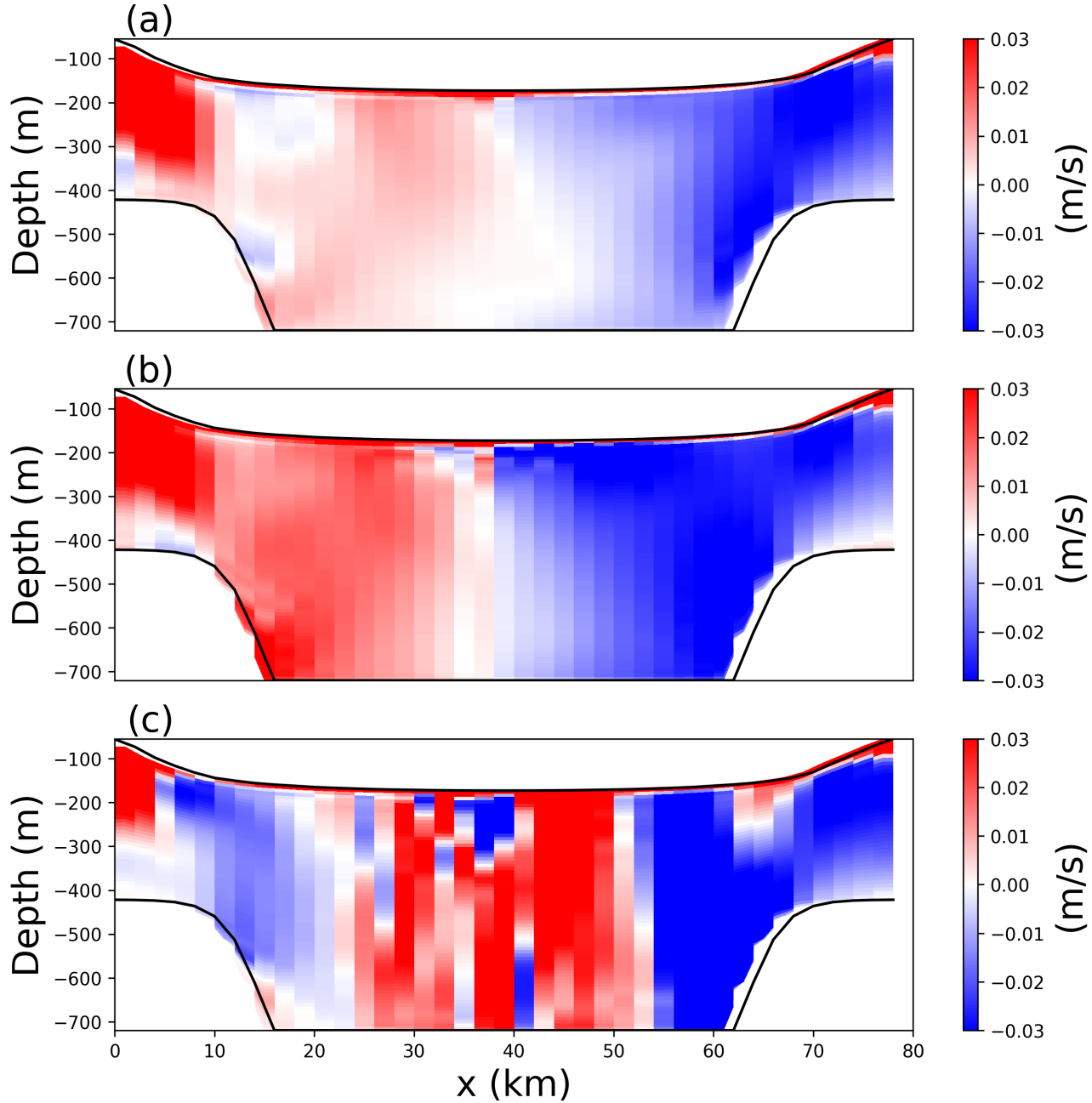


Figure 12. Snapshots of vertical sections of meridional velocity at $y=300$ km in the tabular-iceberg-calving experiment. Snapshots are taken (a) 0, (b) 1, and (c) 50 days after calving. The position of the vertical transects is shown by the blue dashed lines in Figure 2a. Could show 1,14 and 50 days after calving to be consistent with the other Figures. But this figure is more interesting

Parameter	Symbol	Value	Unit
Domain Length	L_x	80	km
Domain Width	L_y	480	km
Horizontal Resolution	Δx	2	km
Number of vertical layers	N_l	72	non-dim
Horizontal Viscosity	ν_H	6.0	$\frac{m^2}{s}$
Diapycnal Viscosity	ν_V	10^{-3}	$\frac{m^2}{s}$
Horizontal Diffusivity	ϵ_H	1.0	$\frac{s}{m^2}$
Diapycnal Diffusivity	ϵ_V	5×10^{-5}	$\frac{s}{m^2}$
Initial Surface Temperature	T_t	-1.9	$^{\circ}C$
Initial Bottom Temperature	T_b	1.0	$^{\circ}C$
Initial Surface Salinity	S_t	33.8	psu
Initial Bottom Salinity	S_b	34.7	psu
Maximum Ocean depth	H_{ocean}	720	m
Relaxation Time of Sponge Layer	T_{sponge}	0.1	days
Time Step for Static Shelf Experiment	dt_{Static}	1000	s
Time Step for Iceberg Calving Experiment	$dt_{Calving}$	10	s

7. Supplementary Figures

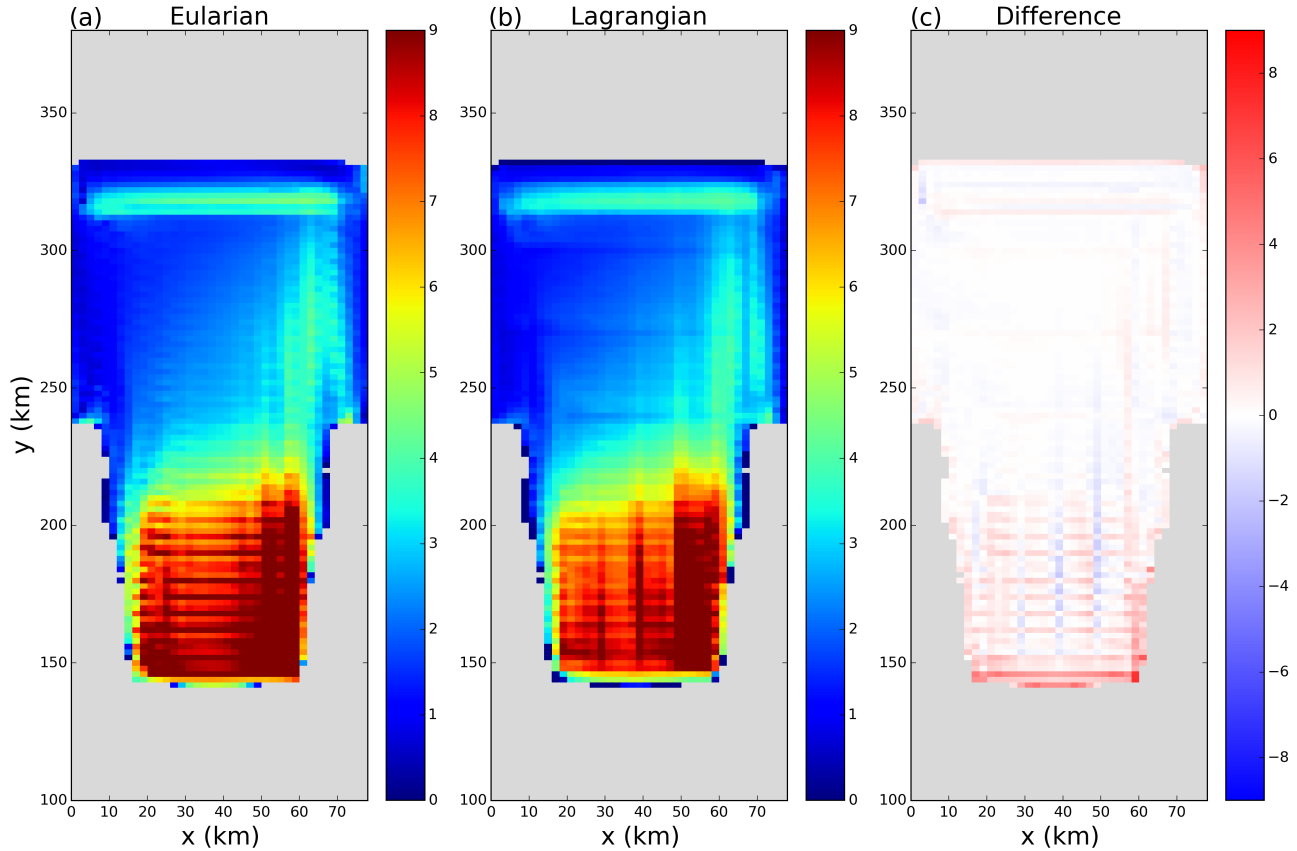


Figure S1. Time-averaged melt rates in the (a) Lagrangian and (b) Eulerian simulations in the static ice-shelf configuration. Panel (c) shows the difference between panels (a) and (b). The time averages are taken over 5 years of model time, beginning at the end of the 5 year spin up period.

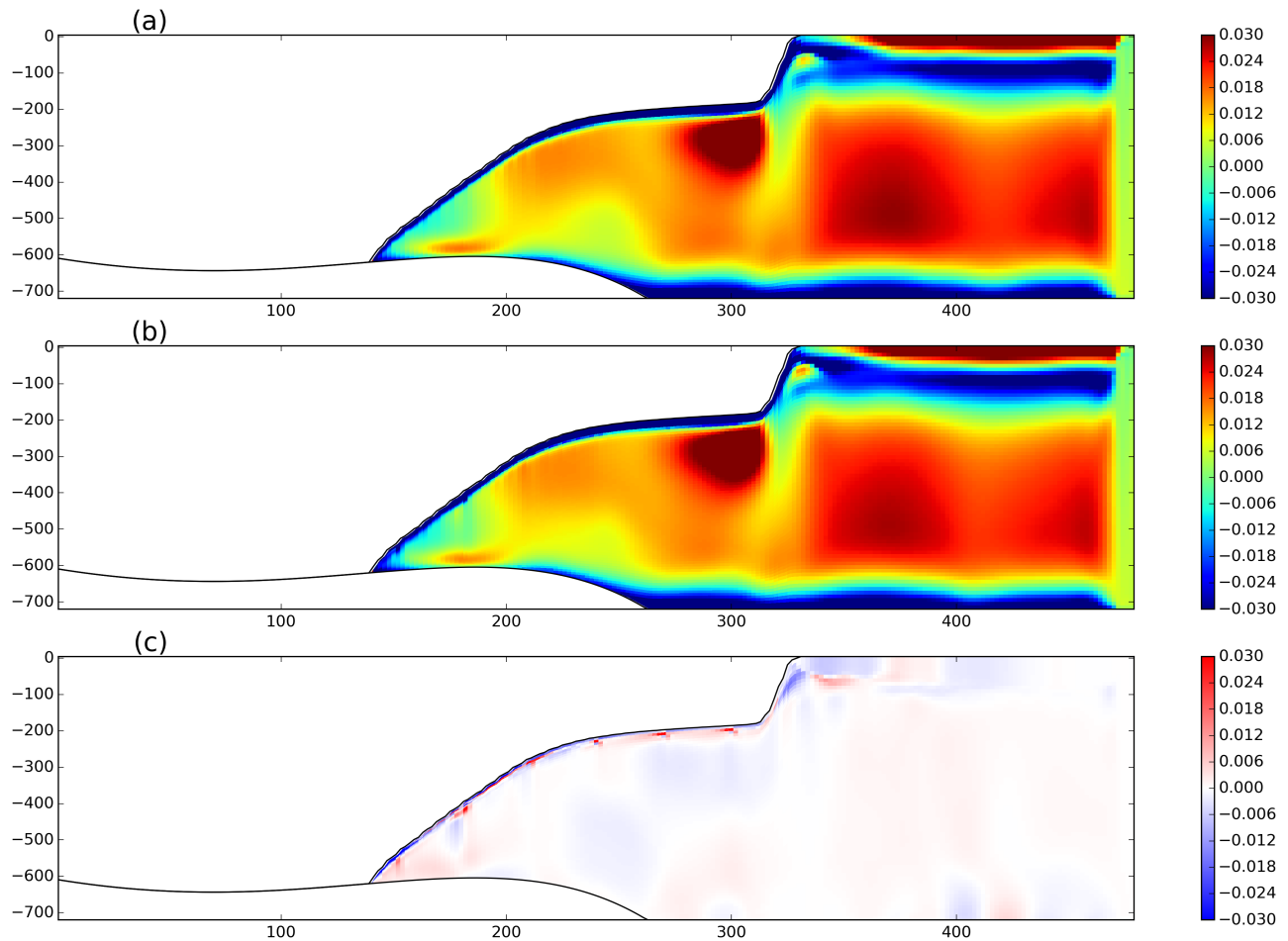


Figure S2. Time-averaged vertical sections of salinity in the (a) Lagrangian and (b) Eulerian simulations in the static ice-shelf configuration at $x=54$ km. Panel (c) shows the difference between panels (a) and (b). The time averages are taken over 5 years of model time, beginning at the end of the 5 year spin up period.

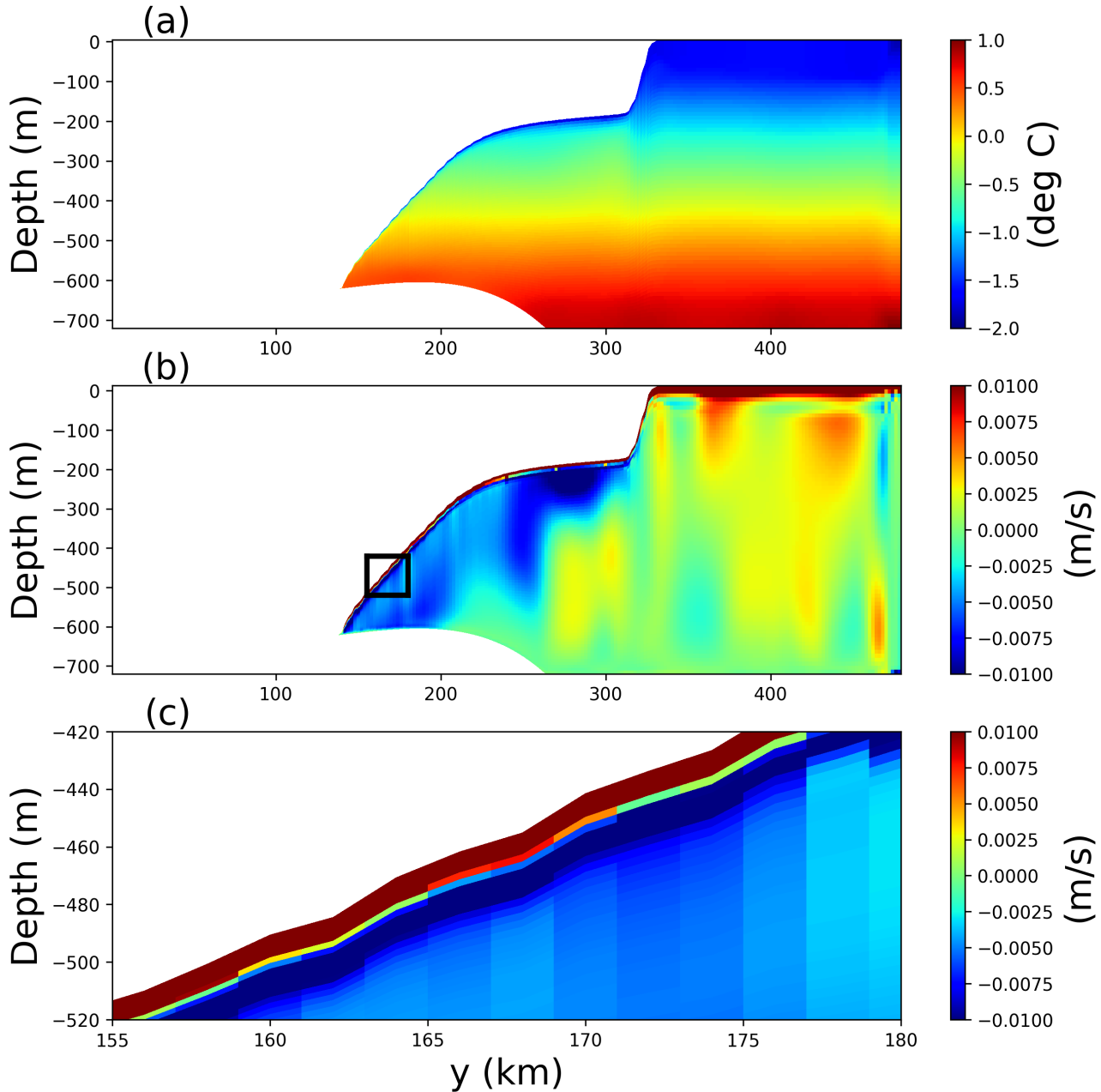


Figure S3. Snapshots of the static ice-shelf experiment taken after 5 years of model simulation, using the Lagrangian ice-shelf model coupled to the MOM6 ocean model. Panels show cross sections of the (a) the steady-state ocean temperature, and (b) the meridional ocean velocity. Panel (c) again shows the meridional ocean velocity, and is zoomed into the region near the ice-shelf base (the zoomed-in region is indicated with a black box (b)).

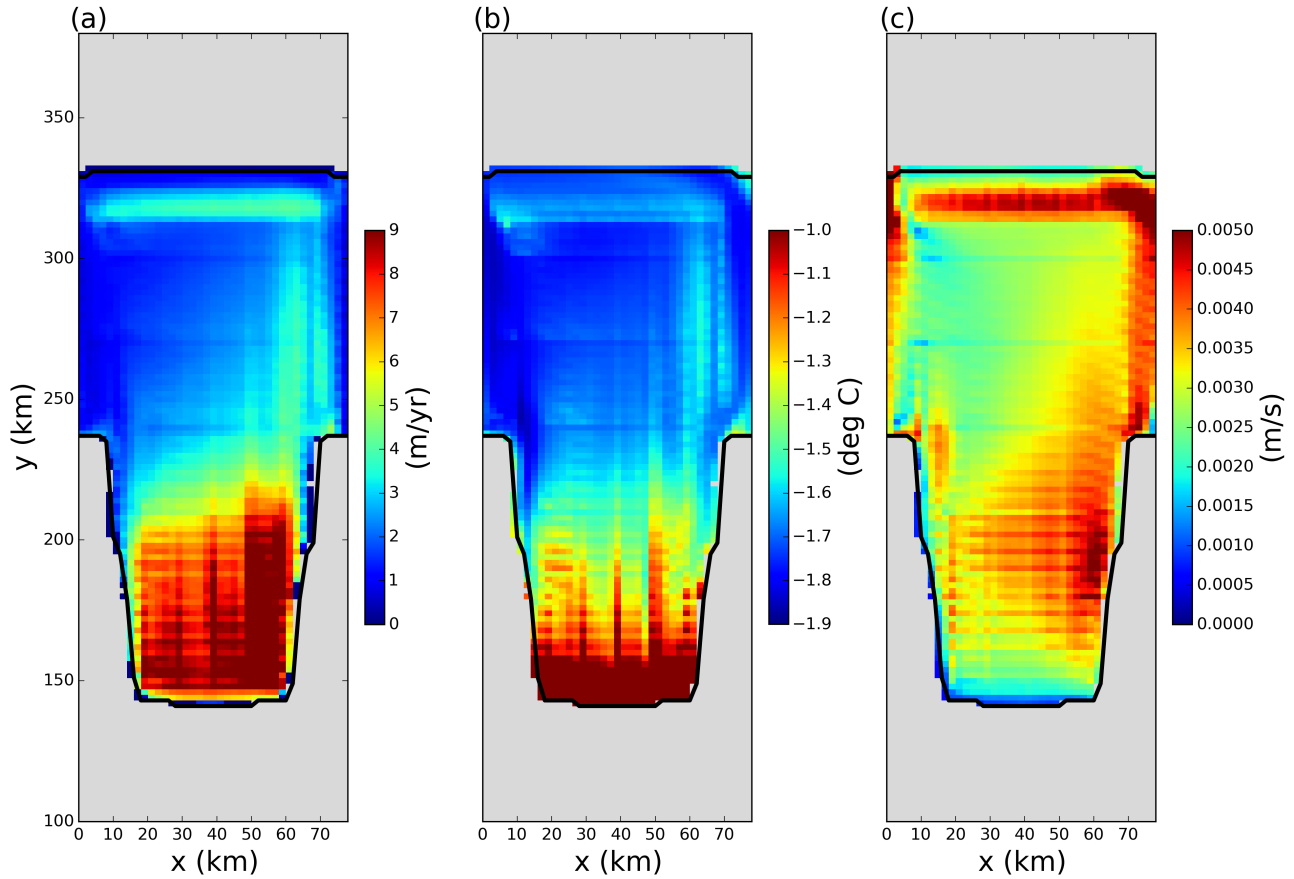


Figure S4. Results of the static ice-shelf experiment using the Lagrangian ice-shelf model coupled to MOM6. The three panels show 5 year time average of the (a) melt rate, (b) top-of-ocean temperature and (c) frictional velocity, u^* , at the base of the ice shelf. Fields are only shown in regions where the ice area fraction is ≥ 0.8 .

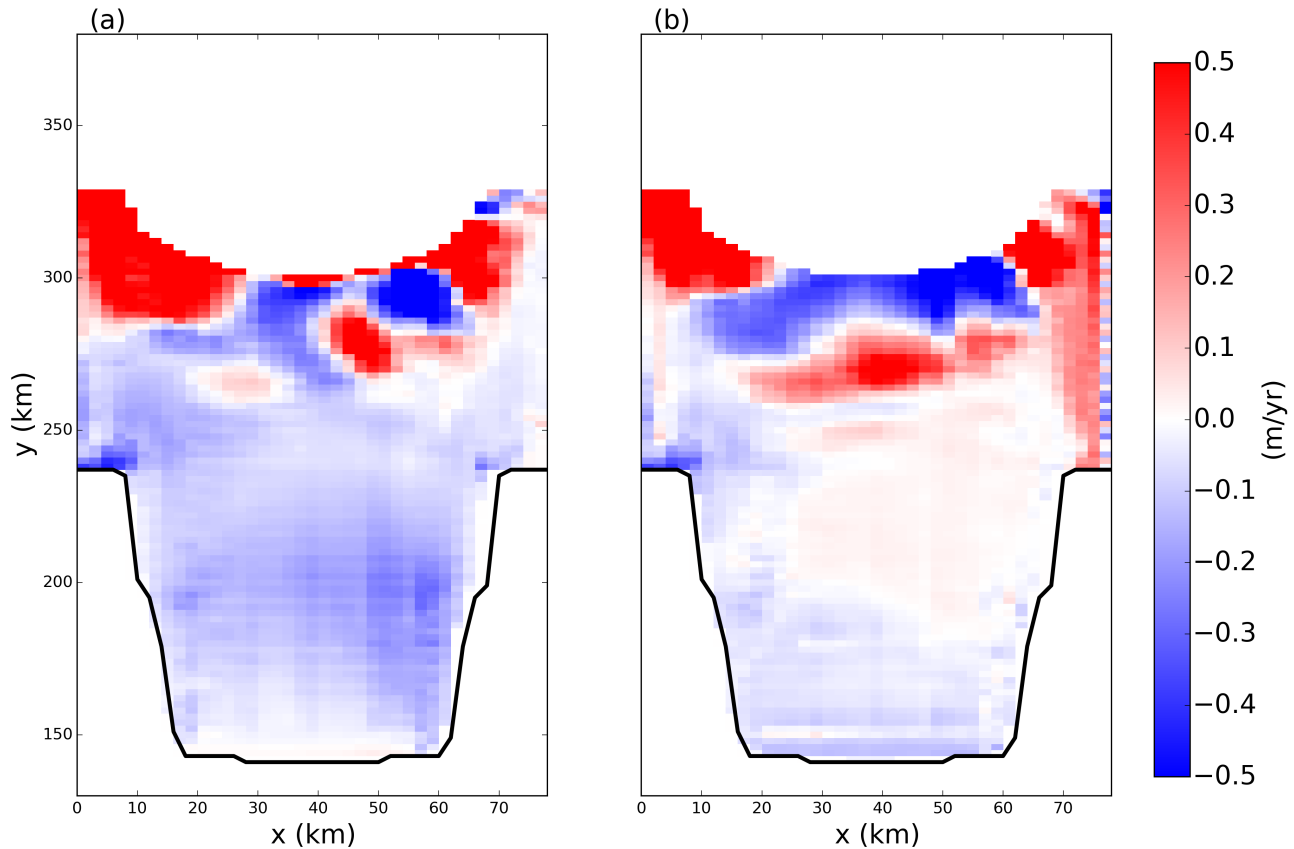


Figure S5. (a) Snapshot of the melt rate at the base of the ice shelf 60 days after the calving event in the tabular-iceberg-calving simulation. (b) Steady state melt rate of the simulation that was spun-up from rest with the semi-circular iceberg removed..

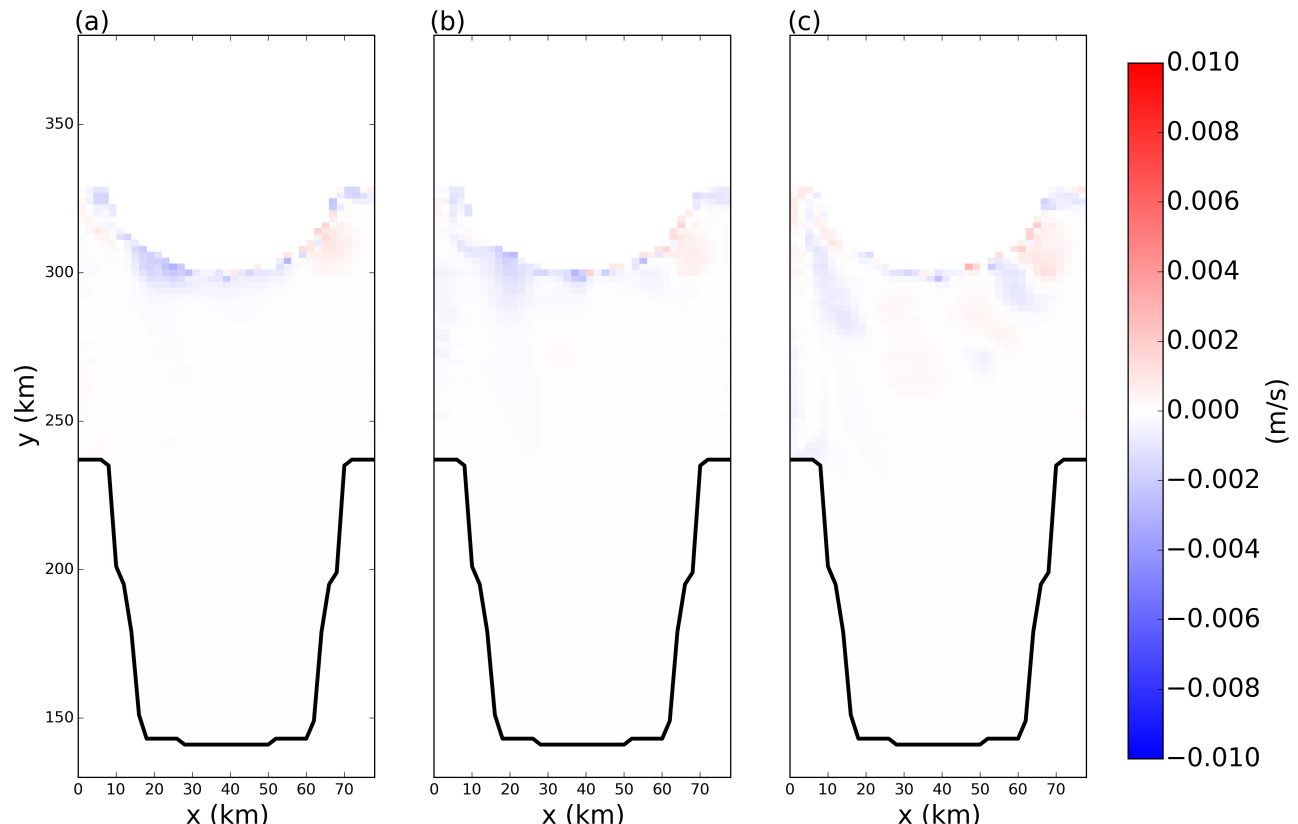


Figure S6. Snapshots of frictional velocity at the ice-shelf base in the tabular-iceberg-calving simulation. Snapshots are taken (a) 7, (b) 15, and (c) 50 days after calving.

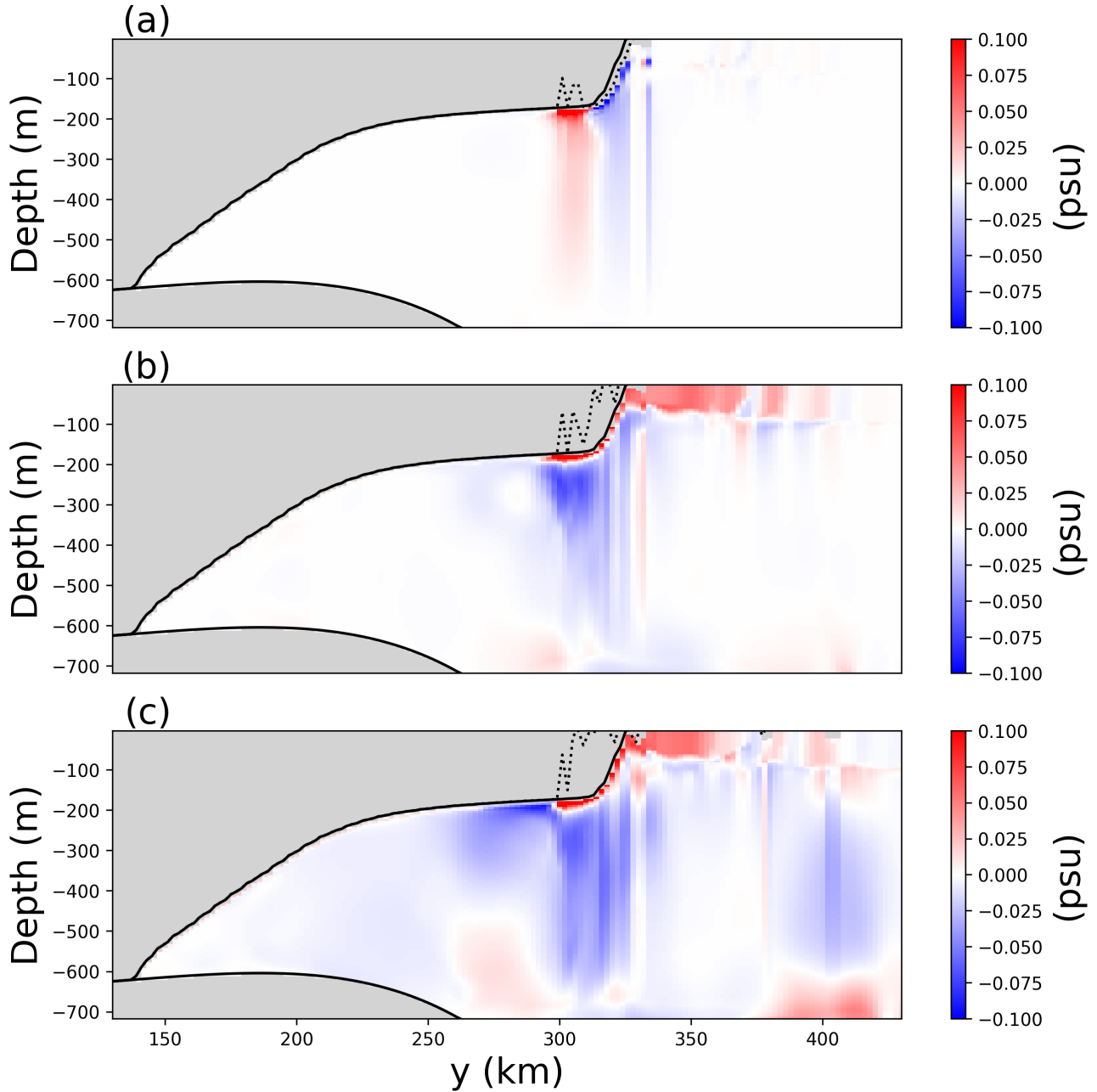


Figure S7. Snapshots of vertical sections of ocean salinity anomaly at $x=40$ km in the iceberg-calving experiment. The anomalies are relative to pre-calving temperatures. Snapshots are taken (a) 1, (b) 15, and (c) 50 days after calving. In each panel, the base of the ice before calving and at the time of the snapshot are shown by the solid and dashed black lines, respectively. Positions that were not the ocean interior at in both snapshots are masked in grey. The position of the vertical transects is shown by the black dashed lines in Figure 2a.